LAWRENCE
LIVERMORE
NATIONAL
LABORATORY

UCRL-JRNL-215701

Material dynamics under extreme conditions of pressure and strain rate

B. A. Remington, P. Allen, E. Bringa, J. Hawreliak, D. Ho, K. T. Lorenz, H. Lorenzana, M. A. Meyers, S. W. Pollaine, K. Rosolankova, B. Sadik, M. S. Schneider, D. Swift, Justin Wark, Barukh Yaakobi

September 27, 2005

Materials Science and Technology

Updated October 14, 2003

UCRL-JRNL-215701

Material dynamics under extreme conditions of pressure and strain rate*

Bruce A. Remington, Patrick Allen, Eduaro Bringa,

Jim Hawreliak, Darwin Ho, K.Thomas Lorenz, Hector Lorenzana,

Marc A. Meyers, Stephen W. Pollaine, Katarina Rosolankova, Babak Sadik,

Matthew S. Schneider, Damian Swift, Justin Wark, Barukh Yaakobi

Fri., Sept. 2, 2005, 9:45 am

Invited paper for a special issue of Materials Science and Technology,

organized by Ron Armstrong and Mark Hull

Abstract

Solid state experiments at extreme pressures (10-100 GPa) and strain rates (~10^6–$10^8 s^{-1}$) are being developed on high-energy laser facilities, and offer the possibility for exploring new regimes of materials science. These extreme solid-state conditions can be accessed with either shock loading or with a quasi-isentropic ramped pressure drive. Velocity interferometer measurements establish the high pressure conditions. Constitutive models for solid-state strength under these conditions are tested by comparing 2D continuum simulations with experiments measuring perturbation growth due to the Rayleigh-Taylor instability in solid-state samples. Lattice compression, phase, and temperature are deduced from extended x-ray absorption fine structure (EXAFS) measurements, from which the shock-induced $\alpha-\omega$ phase transition in Ti and the $\alpha-\varepsilon$ phase transition in Fe are inferred to occur on sub-nanosec time scales. Time resolved lattice response and phase can also be measured with dynamic x-ray diffraction measurements, where the elastic-plastic (1D-3D) lattice relaxation in shocked Cu is shown to occur promptly (< 1 ns). Subsequent large-scale molecular dynamcis (MD) simulations elucidate the microscopic dynamics that underlie the 3D lattice relaxation. Deformation mechanisms are identified by examining the residual microstructure in recovered samples. The slip-twinning threshold in single-crystal Cu shocked along the [001] direction is shown to occur at shock strengths of ~20 GPa, whereas the corresponding transition for Cu shocked along the [134] direction occurs at higher shock strengths. This slip-twinning threshold also depends on the stacking fault energy (SFE), being lower for low SFE materials. Designs have been developed for achieving much higher pressures, P > 1000 GPa, in the solid state on the National Ignition Facility (NIF) laser.

*This work was performed under the auspices of the U.S. Department of Energy by the University of California, Lawrence Livermore National Laboratory under Contract No. W-7405-Eng-48. UCRL-JC-152288-ABS.

I. Introduction

Over the past decade, there has been a surge of activity in the field called extreme materials science or high energy density (HED) materials science. This refers to work being done on HED facilities, such as high energy lasers and magnetic pinch facilities to accesss conditions of extreme pressure, compression, and strain rate (P, ρ/ρ_0, $d\varepsilon/dt$), and make time resolved measurements of the properties. [Asay, 1997; Meyers, 2003; Remington, 2004] One of the long range goals of our work, aimed at the National Ignition Facility (NIF) laser, is to develop the ability to experimentally test models of high pressure, high strain rate material strength, at pressures significantly higher than is achievable by conventional means. This will require achieving the high pressure, solid state conditions, and diagnosing all of the key material quantities. There are a number of challenges to overcome to achieve this goal. Achieving extreme pressures (P >> 1 Mbar) in the solid state is very difficult, all by itself. Extreme pressures can only be generated in small samples, 10-100 μm thick, and can only be maintained for very brief intervals, a few tens of nanoseconds. Yet the pressures have to be applied gently enough in a ramped load that the sample does not shock, because strong shocks generate high temperatures that would melt the sample. Once the extreme pressures are reached, they can only be held for ~10 nsec, during which we need to measure (or at least test models of) strength, and all the quantities that affect it, such as compression, temperature, strain rate, phase, and ultimately dislocation density. In this article, we review our progress towards this overarching goal.

In Sec. II, we review several standard constitutive models for high – (P, $d\varepsilon/dt$) strength, and in Sec. III we describe the "drive" (ie, applied pressure versus time). In

Sec. IV we describe the Rayleigh-Taylor instability experiments being developed to test high pressure models of material strength. The polycrystalline lattice diagnostic of dynamic EXAFS is discussed in Sec. V, and the single-crystal lattice diagnostic of dynamic diffraction is described in Sec. VI. We conclude in Sec. VII with remarks about potential dynamic experiments at extremely high pressures that are being designed for the NIF laser.

II. Constitutive Models

There is a considerable variety of constitutive models for material strength in common use in the material dynamics community. Models such as the Johnson-Cook, [9] Zerilli-Armstrong, [Zerilli, 1987; 1990] Mechanical Threshold Stress (MTS), [Follansbee, 1988] thermal-activation-phonon-drag, [Hoge, 1977; Regazzoni, 1987] Steinberg-Lund, [Steinberg, 1989] Steinberg-Guinan, [Steinberg, 1980] and Preston-Tonks-Wallace [Preston 2003] models are widely, for example. At the high strain rates relevant to the work described in this paper, thermal activation and dislocation glide along slip planes, resisted by phonon drag, are believed to be the dominant (rate determining) mechanisms underlying deformation. [Kochs, 1975; Hoge, 1977; Regazzoni, 1987; Steinberg, 1989] These are illustrated schematically in Fig. 1a. In the thermal activation regime, when a shear stress is applied, dislocations are assumed to be pinned against barriers, until a thermal fluctuation can kick them over the obstacle to glide to the next barrier. In this "jerky glide" regime, [Regazzoni, 1987] the strain rate is given by Orowan's equation, $\dot{\varepsilon} = \rho_m b \bar{u}$, where $\bar{u} = \lambda_b / (t_w + t_g)$ is the average dislocation velocity, λ_b is the average distance between barriers, t_w is the time spent waiting for a

thermal assist, and t_g is the time interval to freely glide to the next barrier. When the dislocations are freely gliding between obstacles at velocity u_g, an equilibrium drag equation gives $\sigma b = D u_g$, where $u_g = \lambda_b / t_g$, σ is the applied deviatoric stress, b is the Burgers vector, and D is the phonon drag coefficient. These two mechanisms can be combined to give a constitutive equation of the form,

$$\dot{\varepsilon} = \frac{\rho_m b^2}{\frac{b}{\lambda_b \nu_a} \exp\left\{\frac{F_0}{kT}\left[1 - \left(\frac{\sigma}{\tau_{MTS}}\right)^p\right]^q\right\} + \frac{D}{\sigma}} \quad . \tag{1}$$

Here, F_0 represents the energy required to push the dislocation over the barrier at T = 0 K, τ_{MTS} corresponds to the mechanical threshold stress, (the stress at T = 0 K required to surmount the peak of the barrier), and p and q represent barrier shape parameters. [Kochs, 1975]

The above discussion assumes rigid dislocations that are undistorted in surmounting a barrier. This assumption is not appropriate for the strong Peierls barriers, σ_P, of a bcc lattice. In surmounting σ_P in a bcc lattice, the dislocation bows considerably, nucleating and propagating a pair of dislocation kinks. [Guyot, 1967] A similar constitutive equation appropriate for a bcc lattice, the Hoge-Mukherjee model, can be written as [Hoge, 1977]

$$\dot{\varepsilon} = \frac{\rho_m b^2}{\frac{1}{\dot{\varepsilon}_0} \exp\left[\frac{2U_k}{kT}\left(1 - \frac{\sigma}{\sigma_P}\right)^2\right] + \frac{D}{\sigma}} \quad , \tag{2}$$

where $\mathbf{1/\dot{\varepsilon}_0 = 2w^2/(La\upsilon)}$. Here, L is the dislocation line length, w the width of the critical pair of kinks, ν the Debye frequency, *a* the separaton between Peierls valleys, and $2U_k$ the energy to form a pair of kinks in the dislocation segment. Note the similarity to Eq. 1 if p=1 and q=2 (in Eq. 1).

An alternate constitutive equation that explicitly includes pressure, temperature, and compression, proposed for extremely high strain rates, is the Steinberg-Guinan model. [Steinberg, 1980] The basis for this model is the assumption that above some critical strain rate, $\sim 10^5$ s^{-1}, all effects due to strain rate have saturated, and material strength becomes independent of strain rate. The only parameters that effect strength in this model are P, T, $\eta=\rho/\rho_0$, and strain, ε. The model is essentially a first order Taylor expansion in pressure and temperature, with a work hardening prefactor, f(ε), and a small correction for compression,

$$\sigma = \sigma_0 f(\varepsilon)\frac{G}{G_0}\ , \qquad \text{(Eq. 3a)}$$

$$\frac{G}{G_0} = 1 + \left(\frac{G_P'}{G_0}\right)\frac{P}{\eta^{1/3}} + \left(\frac{G_T'}{G_0}\right)(T - 300)\ , \qquad \text{(Eq. 3b)}$$

$$f(\varepsilon) = [1 + \beta(\varepsilon_i + \varepsilon)]^n\ , \qquad \text{(Eq. 3c)}$$

where σ_0 and G_0 are the ambient strength and shear modulus, $\eta = \rho/\rho_0$ is the compression, $G_P' = \partial G/\partial P$, and $G_T' = \partial G/\partial T$ are the partial derivatives of shear modulus with pressure and temperature. It is assumed that the rate of change of strength with P and T is the same as that of the shear modulus, G, an assumption that remains unproven at extreme conditions, due to lack of controlled data.

The Steinberg-Lund (S-L) model [Steinberg, 1989] is a combination of the two models just described, and is written

$$\sigma = [\sigma_T(\dot{\varepsilon},T) + \sigma_A f(\varepsilon)]\frac{G(P,T)}{G_0} \qquad \text{(Eq. 4a)}$$

where the thermally activated term, $\sigma_T(\dot{\varepsilon},T)$, is determined by

$$\dot{\varepsilon} = \frac{1}{\frac{1}{C_1}\exp\left[\frac{2U_k}{kT}\left(1-\frac{\sigma_T}{\sigma_P}\right)^2\right] + \left(\frac{C_2}{\sigma_T}\right)^m}, \qquad \text{(Eq. 4b)}$$

and is assumed applicable only when $\sigma \le \sigma_P$. Here, m = 1 corresponds to the standard Steinberg-Lund (S-L) model; other values are discussed below. In its nominal form, the S-L model assumes that $\sigma \approx \sigma_A f(\varepsilon) G/G_0$, when $\sigma > \sigma_P$, which is essentially Eq. 3a, the Steinberg-Guinan, strain-rate-independent model. Note that this essentially prevents phonon drag from being activated. Note also that Eq. 4b is identical with the Hoge-Mukherjee model, Eq. 2, provided that $C_1 = \rho_m L a b^2 \nu/(2w^2) = \dot{\varepsilon}_0$, and $C_2 = D/(\rho_m b^2)$, and m = 1. In Eq. 4, σ_A, C_1, U_k, σ_P, C_2 are all assumed to be constants, and the scaling with P and T is taken into account with the G/G_0 overall factor in Eq. 4a. We can easily write down a "hybrid" form of the S-L model. If, when $\sigma > \sigma_P$, the exponential term in the denominator of Eq. 4b is set to zero, and if the phonon drag term is allowed to activate, this would be similar to the Hoge-Mukherjee model, only with work hardening and pressure hardening (through scaling with the shear modulus) included.

The final model that we describe is the Preston-Tonks-Wallace (PTW) model. [Preston 2003]. In a somewhat simplified form and for low strains, it is written here, , as

$$\sigma_{PTW}(\dot{\varepsilon}) = (2G)\max\{y_0 - (y_0 - y_\infty)\mathrm{erf}[\kappa\hat{T}\ln(\gamma\dot{\varepsilon}_0/\dot{\varepsilon})],\ s_0(\dot{\varepsilon}/\gamma\dot{\varepsilon}_0)^{\beta}\}\ , \quad \text{(Eq. 5)}$$

where, y_0, y_∞, κ, γ, s_0, and β are material constants, and G is the pressure and temperature dependent shear modulus. This model is based on the same mechanisms as the Hoge-Mukherjee or hybrid S-L models above, namely, thermal activation for shear stresses lower than the dominant dislocation barriers, and a viscous drag mechanism for shear stresses above the barriers. At strain rates $d\varepsilon/dt \leq 10^4$, the model is calibrated against Hopkinson bar data and other conventional data. At strain rates $d\varepsilon/dt > \sim 10^9\ s^{-1}$, the model is formulated to reproduce overdriven (strong) shock data, with strength assumed to vary as a power law with strain rate, namely, $\sigma \sim (d\varepsilon/dt)^{\beta}$, with $\beta \approx 1/4$. In the absence of additional data, the region inbetween, "the gap", is bridged by extrapolating the strength curves from these two regimes (thermal activation on the low end, nonlinear drag on the high end) until they meet. Once "gap data" is obtained, it is expected that the PTW model (or at least its nominal input parameters) will be modified accordingly.

We illustrate these models, as a function of strain rate, for one set of conditions (Ta at P = 0.5 Mbar, T = 500 K, and $\varepsilon = 0.1$) in Fig. 1b. The dot-dashed curve labeled (1b) corresponds to the nominal S-L model with its nominal input parameters for Ta. [Steinberg, 1989] The dot-dashed curve labeled (1a) corresponds to the hybrid S-L model, again with nominal Ta input parameters. This latter result is very similar to the curve that would correspond to the Hoge-Mukherjee model, other than the modification

for work and pressure hardening. Curves (1a) and (1b) coincide in the thermal activation regime, that is, for $d\varepsilon/dt <$ a few x 10^5 s^{-1}. Above this strain rate, however, the nominal S-L model transitions essentially to the S-G model, which is strain rate independent, given by curve (1b). The hybrid S-L model, (and also Hoge-Mukherjee), however, allow linear phonon drag to activate, and the strength increases steeply with strain rate, $\sigma \sim d\varepsilon/dt$. Due to the paucity of strength data at these high strain rates, it is unknown which of these two formulations is correct, if either. The solid curve, labeled (3) corresponds to the PTW model, with nominal input parameters for Ta. In the low strain rate regime, $d\varepsilon/dt <$ ~10^5 s^{-1}, PTW also agrees with the S-L model. This is not surprising, since both models were "calibrated" against the same Hopkinson bar data. With nominal input parameters for Ta, the PTW model transitions to phonon drag at a higher strain rate, ~10^8 s^{-1}. So above 10^8 s^{-1}, the PTW model transitions to a "nonlinear phonon drag" model, with a softer dependence on strain rate, $\sigma \sim (d\varepsilon/dt)^{1/4}$, based on overdriven shock data. The hybrid S-L model is shown by curve (2a), in which the attempt frequency, $\dot{\boldsymbol{\varepsilon}}_{\mathbf{0}}$, has been increased by ~100x, the Peierls stress has been scaled by G(P,T), and the phonon drag power law exponent has been set to m = 4. It is apparent that under these settings, the hybrid S-L model is consistent with the PTW model over essentially the entire strain rate range. Curve (2b) shows an intermediate version of S-L, in which the attempt frequency has been increased by a factor of ~40, phonon drag has been turned off entirely, and the Peierls stress has been scaled by G(P,T). Conversely, if the attempt frequency in the PTW model is decreased by a factor of ~1000 (by reducing the parameter gamma), the activation energy increased (by increasing kappa), and the phonon drag power law

exponent (β) increased to ~1, then the PTW model curve (not shown) can be made roughly consistent with the Hoge-Mukherjee curve (1a) in Fig. 1b.

We show the sensitivity of the PTW model to temperature in Fig. 1c for nominal input parameters for Ta, and starting parameters of 0.5 Mbar pressure, compression $\rho/\rho_0 = 1.1$, and plastic strain of $\varepsilon = 0.1$, and nominal temperature of $T_0 = 500$ K. The flow stress versus strain rate is shown, as temperature is increased and decreased by 20% and 40% about its nominal value. The thermal activation regime, here corresponding to $d\varepsilon/dt <$ a few x 10^8 s^{-1}, shows sensitivity to these levels of changes in temperature, but the phonon drag regime is rather insensitive to these levels of changes in temperature. The input parameters to the PTW model, including those for phonon drag, are assumed constant. The phonon drag coefficient should in fact scale as $D \sim (\rho/\rho_0)^{2/3} T^{1/2}$, due to the density of states of the phonon distribution. [Wolfer, 2003; Remington, 2004] This still would leave the phonon drag regime reasonably insensitive to 20-40% variations in temperature. Figure 1d shows a similar scaling, only for 20-40% variations in density. Here, there is little sensitivity in either deformation regime, within the model, due in part, to the assumption of constant input parameters. Hence, in experiments of high pressure, high strain rate material strength, the sensitivity to the exact EOS of the material is not large, and resides in the corresponding temperature uncertainties that could result.

III. Shockless Drive Development

In this section, we discuss the results of an experimental technique for generating a very high pressure "drive" to compress samples in the solid state at high strain rate. This technique has already been experimentally demonstrated up to peak pressures of 200

GPa (2 Mbar) at the Omega laser. [Lorenz, 2005b] Furthermore, radiation-hydrodynamics simulations show that on future facilities, such as the NIF laser, [Paisner, 1994; Hogan, 2001] this technique should be able to drive samples in the solid state to much higher pressures, $P > 10^3$ GPa (10 Mbar). [Remington, 2005b]

We show in Fig. 2 results from this ramped pressure, shockless drive [Edwards, 2004; Lorenz 2005] that has been developed on the Omega laser. [Boehlyt, 1995] The target consists of a low Z, low density reservoir (typically solid density plastic) of nominal thickness ~0.2 mm, followed by a ~0.3 mm vacuum gap, then an Al sample, as illustrated schematically in Fig. 2a. A laser pulse of energy 0.2 – 2 kJ in a temporally square pulse shape of duration 3 – 4 ns is used to drive a strong shock through the low-Z reservoir. When the shock reaches the back side (the side opposite where the laser was incident), the reservoir "explodes" (unloads) into vacuum as a gas of "ejecta". The pressure that is applied to the sample results from the increasing ram pressure, $P_{ram} = \rho_{ejecta} v_{ejecta}^2$, which increases smoothly and monotonically in time as the reservoir unloads, until the reservoir material is depleted. This technique for generating shockless compression was modeled after the early work of Barnes using high explosives (HE) as the source of the shock in the reservoir. [Barnes, 1974; 1980]

The pressure wave is measured with a line velocity interferometer [Celliers, 1998] viewing the back side of a 5-30 μm flat Al sample, typically through a LiF window. An example VISAR image, corresponding to a 5 μm Al sample backed by a ~125 μm LiF window, where P_{max} ~ 1.2 Mbar, is shown in Fig. 2b. [Lorenz, 2005b] The horizontal direction of the image is the "streak" or time direction, and the vertical direction corresponds to the transverse position along the sample. The interference fringes in the

velocity interferometer diagnostic are proportional to velocity, with each fringe shift, δ(fringe position), corresponding to a known velocity increment, δv. Thus, measuring the fringe shift versus time and position on the foil is a direct measure of the velocity of the reflecting surface or interface, if a LiF window is used. As this ramp wave moves through the Al, it eventually steepens into a shock, as illustrated experimentally and numerically in Fig. 2c. The grays symbols are the experimental data, adn the solid curve are radiation-hydrodynamics continuum code simulations. Here, a set of four identical laser shots were done at the Omega laser, each at P_{max} ~ 1.2 Mbar, where the only difference was the Al thickness, which varied over 5 – 33 μm. By the time this 1 Mbar ramp wave has moved through ~30 μm of Al, it has steepened into a shock.

The measured velocity profiles can be back integrated to infer the applied pressure vs. time at the front surface of the Al sample, using a technique developed by Hayes. [24] We show in Fig. 2d the results from five different experiments, varying mainly the laser intensity, leading to peak pressures spanning 0.15 – 2 Mbar. As the peak pressure increases, the pressure rise time decreases. Nevertheless, even at 2 Mbar, with a ~3 ns rise time, the sample is not shocked, at least over the first 10-20 μm of Al. [Lorenz, 2005b]

IV. Material Strength at High Pressure and Strain Rate

To dynamically infer material strength at high (P, dε/dt), hydrodynamic instability experiments have been developed, [Kalantar, 1999; 2000; Colvin, 2003; Lorenz, 2005a; Remington, 2005a] following the technique demonstrated in the early work by Barnes. [Barnes, 1974; 1980] By accelerating a metal sample or payload with a lower density,

higher pressure "pusher", a situation is created where the interface with the payload is hydrodynamically unstable to the Rayleigh-Taylor (RT) instability. Any pre-existing perturbations will attempt to grow, whereas material strength will act to counter or slow this growth. Therefore, by measuring the RT growth of machined sinusoidal ripples in metal foils that are accelerated by the drive, and comparing the observed perturbation growth with that from simulations including a constitutive (strength) model, material strength at high pressure and strain rate may be inferred.

The technique we are developing to test models of high pressure, dynamic strength (such as represented by Eqs. 1-5) is to measure the RT-induced growth of ripples with time-resolved face-on radiography, as illustrated schematically in Fig. 3a. We use the ramped pressure drive discussed in Fig. 2 to generate both high pressure conditions in the sample of interest, and to accelerate the sample. Preimposed ripples on the side of the metal sample facing the reservoir then are induced to grow due to the RT instability, that is, the RT instability exerts a shear stress on the sample, which tries to generate plastic flow from the thin regions or valleys of the perturbations (RT "bubbles") to the thick regions or peaks of the perturbations (RT "spikes"). The material strength at the generated high pressures attempts to resist this plastic flow. Hence, the rate at which the ripples grow is sensitive to the material strength; the stronger the material, the lower the expected RT growth rate. Comparing 2D hydrodynamic simulations, including a strength model, with the observed RT growth rates, then allows the model to be tested, and the high pressure strength to be deduced.

Figure 3b shows results from such an RT experiment, in this case, for Al6061-T6 foils at $P_{max} \sim 200$ kbar. The data for perturbation growth factor versus time are given by

the plotting symbols, and the results of the 2D simulations, using the Steinberg-Guinan strength model (Eq. 4) are given by the solid curves. The pressure hardening parameter, $\mathbf{A = \frac{1}{G_0}\frac{\partial G}{\partial P}}$, is varied in the model until the simulations reproduce the observations. At peak pressure, then, the deduced strength from the best fit simulation, is 10.5 kbar, at P_{max} ~ 200 kbar and peak strain rate of ~6 x 10^6 s^{-1}. [Lorenz, 2005a] Using the simulation that reproduced the experimentally observed RT growth shown in Fig. 3b, we then show in Fig. 4 the time histories of pressure (Fig. 4a), temperature (Fig. 4b), equivalent plastic strain (Fig. 4c), and flow stress (Fig. 4d). The results have been volumetrically averaged with e^{-kz} weighting (where $k = 2\pi/\lambda$ corresponds to the perturbation wave number). This particular weighting is based on the recognition that the strength that matters is that in the vicinity of the growing ripples. Since RT induced ripples penetrate the foil a distance of order e^{-kz}, where $k = 2\pi/\lambda$ is the perturbation wave number, we have used e^{-kz} weighting in the averages shown in all the plots in Fig. 4. The average peak pressure (Fig. 4a) was ~200 kbar with a ~6 ns rise time. The temperature starts out a room temperature, and increases to a peak value of ~400 K. The equivalent plastic strain from the simulation is shown in Fig. 4c, and asymptotically reaches $\varepsilon_p \sim 0.2$. By looking at the average values of the slope at various time intervals, average plastic strain rates can be estimated. Early in time (40-55 ns), the average strain rate is $\langle d\varepsilon_p/dt \rangle \sim 6 \times 10^6$ s^{-1}. At later times, 55-70 ns, as the applied pressure drops off, the strain rate also decreases, $\langle d\varepsilon_p/dt \rangle \sim 3 \times 10^6$ s^{-1}. At still later times, 70-90 ns, the strain rate approaches $\langle d\varepsilon_p/dt \rangle \sim 1 \times 10^6$ s^{-1}. The volume averaged strength is shown in Fig. 4d. The peak value is 10.5 kbar, which is a factor of 10.5/2.9 ~ 3.5 larger than the strength at ambient conditions, due largely to the

pressure hardening effect. This is the approach we are pursuing to test high pressure, high-strain-rate models of material strength, and extremely high pressures.

V. Dynamic EXAFS experiments

We now discuss a time-resolved microscale diagnostic developed to probe the local (short range) lattice response, namely, dynamic EXAFS (extended x-ray absorption fine structure). This EXAFS technique probes the lattice short range order, and works both with polycrystalline or single crystal samples, and offers the potential to infer phase, compression, and temperature of the loaded sample, with sub-nsec time resolultion. The basis for this diagnostic is illustrated in Fig. 5a. [Konningsberger, 1988; Lee, 1981; Rehr, 2000] When an atom absorbs an ionizing, high energy x-ray, an electron rises from a bound state into the continuum. The outgoing wave packet of the free electron, illustrated by the concentric solid circles in Fig. 5a, scatters off of neighboring atoms, as illustrated by the dashed circular curves. The outgoing and reflected waves interfere with each other. The square of the total electron wave function is what determines the probability of the process, and this interference is therefore observed in fine structure in the x-ray absorption just above an opacity edge. For K-edge absorption, the standard EXAFS equation can be written, in terms of the normalized absorption probability, as [Konningsberger, 1988; Yaakobi, 2003; 2004a; 2004b]

$$\chi(k) = \Sigma_j \frac{N_j}{kR_j^2} F_j(k) \sin\{2kR_j + \phi_j(k)\} e^{-2\sigma_j^2 k^2} e^{-2R_j/\lambda(k)} \quad , \qquad (9)$$

where $\chi(k) = [\mu(k) - \mu_0(k)] / \mu_0(k)$, and $\mu_0(k)$ represents the smooth absorption above the edge corresponding to an isolated atom (no interference modulations). The summation is over coordination shells, N_j is the number of atoms in the shell, and R_j its radius. The $F_j(k)$ factor corresponds to the backscattering amplitude for the electron wave function reflected from the jth coordination shell. The $\phi_j(k)$ represents a phase shift due to the electron wave packet moving through a varying potential. The exponential, $e^{-2\sigma_j^2 k^2}$, represents the Debye-Waller factor, which reduces the coherent interference of the EXAFS signal due to thermal fluctuations in the local scattering atoms. The $e^{-2R_j/\lambda(k)}$ factor represents the attenuation of the electron wave function due to the finite mean free path, $\lambda(k)$, of the ejected electron.

We have developed the time-resolved EXAFS diagnostic technique at the Omega laser. [Yaakobi, 2003; 2004a; 2004b] The experimental setup is shown in Fig. 5b. Three 1-ns-square laser beams stacked back to back to make a 3-ns-square drive pulse are used to shock compress the sample being studied. In Fig. 5b, this corresponds to a 10 μm thick sample of polycrystalline Ti embedded in 17 μm thick CH on either side, and the remaining 57 beams implode an inertial confinement fusion (ICF) capsule. This implosion generates a short (~120 ps) burst of smoothly varying hard x-rays, $I = I_0 \exp(-E_x/T)$, to be used for the EXAFS absorption, as shown in Fig. 5c. Typical values for the implosion x-ray spectrum are $I_0 = 2\text{-}3 \times 10^{19}$ keV/keV and T = 1.25 keV. A measured raw EXAFS absorption spectrum showing the modulations just above the K-edge for room temperature, unshocked polycrystalline Ti is shown in Fig. 5d. [Yaakobi, 2003]

EXAFS measurements from shocked polycrystalline vanadium at $P_{shk} \sim 400$ kbar, together with EXAFS theoretical fits, using the FEFF8 code, [Rehr, 2000; Yaakobi,

2004a; 2004b] are shown in Fig. 6a. Vanadium was picked as a good reference material, since it is not expected to undergo any phase transition at shock pressures < ~1 Mbar. The fits of the shocked V EXAFS data with the FEFF8 code shown in Fig. 6a are very good, and suggest a compression of ~15% and shock temperature of ~800 K. Both the shock compression and shock temperature thus inferred are in good agreement with predictions with radiation-hydrodynamics code simulations using the LASNEX code. [Zimmerman, 1975]

Having established the technique of dynamic EXAFS to diagnose shocked samples with sub-nsec time resolution, we then applied the technique to shocked polycrystalline Ti, at the same P_{shk} ~ 400 kbar, as shown in Fig. 6b. In this case, the situation is distinctly different from the shocked V. If we assume that the shock temperature is the same as for shocked V, and fit the FEFF8 simulation to reproduce the modulation period, assuming no phase transition, the result is shown in green. This fit is clearly unsatisfactory, and suggests this interpretation cannot be correct. If we again assume no phase transition, but arbitrarily increase the temperature until the theoretical curve fits the data, the resulting temperature is T ~2100 K. This temperature is over a factor of two higher than predicted with the LASNEX simulations, and in distinct disagreement with the temperatures inferred from the shocked V at the same shock strength. We concluded that such a high temperature is unphysical. If, on the other hand, the shocked Ti has undergone the $\alpha - \omega$ phase transition, as expected for these pressures, and assuming the nominal shock temperatures from the radiation-hydrodynamics simulations of T ~900 K, the result is shown by the red curve in Fig. 6b. The agreement with the data is excellent, and we therefore conclude that this is the most likely

interpretation. We thus conclude that, at $P_{shk} \sim 400$ kbar, the time scale for the $\alpha-\omega$ phase transition is prompt, $\delta t_{\alpha-\varepsilon} < 1$ nsec.

We next looked at shocked polycrystalline Fe with this dynamic EXAFS technique. [Yaakobi, 2005a, 2005b] We first used the FEEF8 theory to establish the expected EXAFS spectra for unshocked α-phase (bcc) Fe and shocked ε-phase (hcp) Fe, assuming a ~20% compression for the shocked state, as shown in Fig. 6c. A 20% compression is predicted from radiation-hydrodynamics simulations of shocked Fe at $P_{shk} \sim 350$ kbar, assuming the α - ε phase transition. Figure 6c clearly shows that the small peak marked "w" disappears in the ε-phase. The dynamic EXAFS results of the shocked Fe experiments are shown in Fig. 6d; the "w"peak is unmistakenly absent. Based on the comparison of Figs. 6d with 6c, we conclude that we have observed the α - ε phase transition of shocked Fe, and that the transition time scale (at $P_{shk} \sim 350$ kbar) is sub-nsec. [Yaakobi, 2005a, 2005b] Dynamic diffraction experiments of shocked Fe also at the Omega laser, have also shown that this transition occurs on sub-ns time scales at $P_{shk} \sim 350$ kbar. [Kalantar, 2005] In addition, the shocked Fe diffraction experiments showed that the compression path was from 1D α-phase (bcc) to 3D ε-phase (hcp), with no observation of a 3D, plastically relaxed α-phase preceding the phase transition. The earlier MD simulations had actually predicted this exact lattice response. [Kadau, 2002]

VI. Dynamic diffraction experiments

We now discuss time-resolved dynamic diffraction experiments. This technique offers the potential to probe fundamental quantities such as phase, Peierls barrier, and dislocation mobility, at high pressures and strain rates, and is particularly well suited to

studies of shocked, single crystals. If a shock or compression wave traverses a single crystal, the lattice planes compress, and potentially relax through plastic flow towards a more 3D symmetric (hydrostatic) configuration. This can be observed by recording Bragg diffraction signals off multiple lattice planes, as illustrated in sketch in Fig. 7a. The shock compressed lattice can be measured by recording the diffraction signal from a short (~1 ns) synchronized point source burst of x-rays, onto x-ray film. An example of an unshocked diffraction experiment in single crystal Cu, done at the Vulcan laser at RAL, England, is shown in Fig. 7b. [Hawreliak, 2005] The (laser driven) x-ray source was Cu He_{α} at 8.3-8.4 keV. Also shown are the fits, with lattice planes identified. Even though this is unshocked, the image in Fig. 7b shows the power of dynamic diffraction for determining the phase of the sample, with sub-nsec time resolution. We have also done dynamic diffraction experiments with shocked Cu, at $P_{shk} \sim 180$ kbar [46] The conclusion from the dynamic experiments was that the shocked Cu sampled relaxed to a 3D-symmetric (hydrostatic) state promptly, ie, over sub-nsec time scales. We show an example from a dynamic (driven) experiment in Fig. 7c for single crystal Ti shocked along the [0001] direction at $P_{shk} \sim 70$ kbar, done on the Janus laser at LLNL. [Swift, 2005] Initially there is diffraction only from the unshocked region (lower arc, labeled "ambient"). Later in time, there are regions of the Ti that have been shocked, and regions that remain unshocked. With a laser driven, doubled pulsed "backlighter" (ie, timed burst of x-rays), both shocked and unshocked regions can be superposed on the same film pack, as shown in the image in Fig. 7c. Ongoing dynamic diffraction experiments over a range of shock strengths are attempting to confirm the $\alpha-\omega$ phase transition inferred from the dynamic EXAFS results. The diffraction experiments are also examining whether the

compression is in a plastically relaxed 3D symmetric (~hydrostatic) state prior to the phase transition. [Lorenzana, 2005]

Molecular dynamics (MD) simulations offer a very powerful tool for predicting the microscopic lattice response to compression at high pressures and strain rates. We show two examples in Fig. 8, corresponding to shocked Cu (Figs. 8a, 8b) and shocked Ti (Figs. 8c, 8d). The shocked Cu simulation corresponds to a 350-milliion atom simulation of single crystal Cu ~1 μm thick, shocked at P_{shk} ~ 35 GPa along the [001] direction. [Bringa, 2005b] The Cu sample included pre-existing dislocation sources in the form of prismatic loops, and the shock front had a ~50 psec linear ramp. A snapshot from this simulation at 100 ps, showing the centro-symmetry parameter (CSP), is given in Fig. 8a. The color scale has been adjusted to show both dislocations and stacking faults. The shock leading edge is just approaching the pre-existing prismatic loop source at the upper right of the figure. Once the pressure ramp wave exceeds the threshold for either activating the source (σ_{zz} ~ 10 GPa) or homogeneous nucleation of dislocations, σ_{zz}~30 GPa, a high density of dislocations and stacking faults is created, and the evolution towards 3D plastic relaxation behind the shock front commences. One conclusion from these simulations is that to reproduce the experimentally observed prompt 3D plastic relaxation of shocked, single crystal Cu, [46] requires very large scale simulations, covering ~1 μm sample thickness and ~0.2 ns shock transit time. Shorter simulations show large dislocation densities being created, but do not allow sufficient time for dislocation transport to relax the initially 1D lattice compression to the plastic, 3D relaxed state. [Rosolankova, 2004] The dislocation density versus position, for a full set of time steps, from the simulation illustrated in Fig. 8a is shown in Fig. 8b. Prior to the

shock wave encountering the pre-existing source, the dislocation density and relaxation corresponds to homogenous nucleation, and the dislocation density from the MD simulation is ~10^{14} cm^{-2}. Once the pre-existing source has been activated by the ramp wave, the dislocation density drops by a factor of ~3, due to plastic relaxation commencing at a much lower stress threshold of ~10 GPa. This allows greater time for plastic relaxation to occur during the ramp, and hence, the lower peak value of dislocation density. [Bringa, 2005b]

In Fig. 8c, we show an MD simulation of shocked single crstal Ti, at a shock strength of P_{shk} = 22 GPa = 220 kbar, which is well above the experimentally inferred 12 GPa shock threshold for observing the α–ω phase transition. [Yaakobi, 2004a; 2004b] The Ti was shocked along the [0001] direction. The MD shows a very prompt transition from the α-phase to the ω-phase. Figure 8d shows axial profiles of the pressure wave, showing a dramatic 3-wave structure. The leading elastic (1D compression) wave is observed in this plot at a position of ~300 Angstroms, followed by a plastic relaxation wave at ~290 Angstroms. The α–ω phase transition wave trails these two leading waves, commencing at a position of ~200 Angstroms. This situation, which is consistent with the experimental diffraction results shown in Fig. 7d, is different from the shocked Fe case, which evolved directly from 1D compression of the initial phase directly into the phase transition. With the shocked Ti, it appears that the lattice first enters the plastic relaxation regime, then undergoes the structural phase transition. It will be interesting in subsequent work, to understand the precise differences between these two cases.

VII. Recovery of Driven Samples

In this section the use of sample recovery to infer deformation mechanisms and integral quantities about the drive and sample are discussed. The experimental configuration for one class of recovery experiments is shown in Fig. 9a. In the ramped drive case illustrated, the laser drives a shock through a reservoir, which expands across a gap, and stagnates on the sample being studied, similar to the drives illustrated in Fig. 2. The main differences are that the sample is typically much thicker so that it survives the loading process, and it is recovered in a foam filled recovery tube. A substantial number of recovery experiments have also been done with a simpler, shock drive that results from direct laser illumination of the sample. [Schneider, 2004; Meyers, 2003; McNaney, 2004] In the ramped wave case, as the compression wave runs into the sample, it eventually steepens into a shock, as shown in Fig. 2c. So for recovery experiments involving thick samples and a ramped drive, the portion of the sample nearest the driven surface feel the ramped (shockless) loading, whereas regions deeper into the sample see a shocked drive. The lattice response can vary, depending on whether the load is a ramp or a shock. [McNaney, 2005]

In either loading case, the macroscopic end result is the formation of a crater at the driven surface. An example for single crystal Cu ramp loaded to $P_{max} \sim 250$ kbar, is shown in Fig. 9b. [McNaney, 2005] The crater dimensions are ~120 μm deep by ~1 mm diameter, and depend on the strength and duration of the loading, and the strength of the material. The dynamics of crater formation are illustrated in Fig. 9c, based on the results from 2D simulations. Note in particular that the crater formation process is very slow, compared to the loading. The duration of the high pressure (250 kbar) loading is a few

tens of nanoseconds. Behind the loading wave, a slow plastic flow is induced. This plastic flow continues until its energy is dissipated by the strength of the material. The result is that the crater formation is not complete until a microsecond or longer, as shown in Fig. 9c. The temperatures felt, as a function of depth from the loaded surface, are shown in Fig. 9d, from the same simulations that reproduced the observed crater depth. In the shockless region, at depths < ~100 μm, the peak temperature remains below ~400 K. Deeper in, > 100 μm, the ramped wave has steepened into a shock, and the peak temperature is slightly above 400 K. The high temperature conditions decay away over time intervals of ~100 nsec. The short duration of the high pressure and high temperature conditions is thought to allow the dynamically created microstructure (dislocations, stacking faults, twins, etc) to be more effectively "frozen in", such that the residual microstructure is more closely correlated to the microstructure created dynamically. In comparison, HE loaded samples typically have high pressure conditions lasting a microsecond or longer, and the high temperature conditions last longer yet. Under the HE loaded conditions, considerable annealing, thermal recovery, and recrystallization is thought to occur, making the interpretation of the residual microstructure more problematic, especially for very high pressure loading conditions. [Cao, 2005]

Examples of our results are shown in Fig. 10 for single crystal, thick Cu shocked along the [001] direction. [35, 36, 42, 43] Samples of ~1 mm thick single crystal Cu were shock compressed along the [001] direction by laser illumination with 40 - 320 J of laser energy in a 3.5 ns pulse in a 2.5 mm diameter spot on the Omega laser. The samples were recovered from a foam-filled recovery tube, sectioned, and analyzed by TEM. The image shown in Fig. 9a shows the residual microstructure resulting from a ~12 GPa

shock, and the image in Fig.9b corresponds to a ~40 GPa shock, along the [100] crystal orientation. The dislocation cell structure shown in Fig. 9a corresponds to the residual tangled dislocations that result from shock deformation due to slip along the 12 dominant slip systems: four {111} planes and three <110> slip directions within each of these planes. The residual microstructure shown in Fig. 9b is considerably different from that shown in Fig. 9a. This image is the result of a TEM analysis with an electron beam direction of B = <001>, and the (electron) diffraction plane corresponds to (200). The distinct cross-hatch pattern represents traces of {111} planes on (001), that is, the edge-on view of the four {111} planes cutting the (001) plane. The different hues in the criss-cross pattern represents stacking fault bundles or regions of micro-twins. All four stacking fault variants, $(111)\frac{1}{6}[\bar{1}\,\bar{1}\,2], (11\bar{1})\frac{1}{6}[112], (\bar{1}\,11)\frac{1}{6}[1\bar{1}\,2], (1\bar{1}\,1)\frac{1}{6}[1\bar{1}\,2]$, are observed (that is, a displacement of $\frac{1}{6}[\bar{1}\,\bar{1}\,2]$ due to a residual partial dislocation, along the (111) slip plane, and so on). Given that the laser-induced shock direction was <001>, all four {111} primary slip planes should be activated with equal probability, having the same Schmid factor of 0.4082. [35] The comparison between the residual dislocation cells shown in Fig. 9a and the micro-twins shown in Fig. 9b suggests a twinning shock threshold between 12 GPa and 40 GPa. This threshold can be estimated analytically, as described in [36], giving $P_{twinning} \approx 17$ GPa.

This slip-twinning threshold in Cu is sensitive to other factors as well. When the orientation along which the single crystal Cu is shocked is changed from [001] to [134], the slip-twinning threshold increases considerably, as shown in Fig. 9c. When shocked at 40 GPa along [134], the dominant deformation mechanism is still apparently slip. [35; Schneider, 2005a] The suggestion is that there are fewer slip systems activated when Cu

is shocked along [134]. This results in a lower probability of dislocation tangles and pinning sites, lowering the density of forest dislocations, and allowing slip (by dislocation transport along glide planes) to occur to higher shock pressures and strain rates. The deformation mechanism can also be modified by lowering the stacking fault energy, thus making twinning energetically more competitive with slip. Figure 9d shows the residual stacking faults and microtwins in Cu(6 wt.% Al), shocked along the [001] direction at P_{shk} ~ 12 GPa. When alloyed with 6 wt.% Al, the stacking fault energy has been lowered sufficiently that stacking fault bundles and twinning are the preferred deformation mechanism at P_{shk} ~ 12 GPa, (Fig. 9d) whereas for pure Cu shocked in the same manner (Fig. 9a), slip was the dominant deformation mechanism. [Schneider, 2005b]

In Fig. 10e, the results of an analytic model, which has been "calibrated" against experiment, is shown, for predicting the slip-twinning threshold shock pressure for single crystal Cu shocked along the [001] or [134] directions, as a function of temperature. [Schneider, 2004] As already discussed, this threshold is expected to be higher for the [134] direction, which is reflected in the analytic prediction in Fig. 10e. At high temperature, however, slip becomes a more favorable deformation mechanism, which is why the curves have a positive slope.

We conclude with a figure showing the residual dislocation density for Cu(2 wt. % Al) and Cu(6 wt. % Al), as a function of shock pressure. Since the Cu(2 wt% Al) has a higher slip-twinning threshold, dislocation transport will be the dominant mechanism to higher shock pressures, which is why this system has the higher residual dislocation density. Nonetheless, the peak observed residual densities, $\sim 10^{14}$ m^{-2}, is several orders of magnitude lower than what is thought required immediately behind the shock front to

releave the shear stress, as predicted by the MD simulations shown in Fig. 8b. It is thought that during decompression, and due to thermal healing, that the residual dislocation density is much lower, at least 100x (maybe more) than the dynamic dislocation density required to relax the shear stress directly behind the shock front. [Bringa, 2005c]

VIII. Experiments Planned for the NIF Laser

Up until now, we have described experiments that have been done on existing laser facilities. Pressures and strain rates achieved correspond to 10-200 GPa and 10^6-10^8 s^{-1}. With the commissioning of the new National Ignition Facility laser at LLNL, [Paisner, 1994; Hogan, 2001] an opportunity presents itself to increase the pressures of the samples in the solid state to much higher values, $P > 10^3$ GPa. [Remington, 2005b] It will be particularly interesting to see, for example, how Peierls barrier, shear modulus, and material strength scale as pressure and strain rate are increased 100-fold above 10 GPa and 10^5 s^{-1}. At the other extreme for laser experiments, sample sizes approaching ~1 cm in transverse dimension and ~1 mm in thickness at pressures of a few x 100 GPa may be possible, using much larger laser spots and much longer (~100 ns) pulse lengths.

In summary, the field of extreme materials science is gaining considerable interest, and new results are emerging at a fast pace. In this article, we have review the progress of our working group in this area. All of the experiments discusses in this paper were done on various high energy lasers, such as the Janus, Trident, Vulcan, and Omega lasers. High strain rate constitutive (strength) models were presented, showing that a key observable will be the transition from the thermal activation to phonon drag regime. A

ramped, shockless drive was developed, to allow high pressure regimes in the solid state to be accessed. Rayleigh-Taylor hydrodynamics experiments were demonstrated to be sensitive to high (pressure, strain rate) strength models. The EXAFS diagnostic technique allows a volumetrically averaged temperature, compression, and phase to be experimentally determined. Dynamic diffraction experiments allow phase and compression to be measured, and also allow the rate of the 1D-to-3D transition to be followed, which is sensitive to the dislocation density and mobility. MD simulations were shown that were in very good agreement with EXAFS and diffraction experiments of shocked samples. Recovery and analysis of the residual microstructure was shown to allow the dominant deformation mechanism to be inferred, and in same cases "controlled". Dislocation densities predicted from the MD simulations are significantly higher than those observed in the residual microstructure. A very important diagnostic need for future experiments will be a dynamic, time-resolved, dislocation density diagnostic.

REFERENCES

* This work was performed under the auspices of the U.S. Department of Energy by UC,

Lawrence Livermore National Laboratory under Contract No. W-7405-ENG-48.

[Asay, 1997] Asay Int. J. Impact Eng. 20, 27-61 (1997).

[Barnes, 1974] J.F. Barnes, P.J. Blewett, R.G. McQueen, K.A. Meyer, and D. Venable, *J. App. Phys.*, 1974, Vol. 45, 727;

[Barnes, 1980] J.F. Barnes, D.H. Janney, R.K. London, K.A. Meyer, and D.H. Sharp, J. Appl. Phys., 1980, Vol. 51, 4678.

[Boehly, 1995] T. H. Boehly, R. S. Craxton, T. H. Hinterman et al., *Rev. Sci. Instrum.*, 1995, Vol. 66, 930.

[Bringa, 2005a] Bringa et al., Nature, submitted (2005).

[Bringa, 2005b] Bringa et al., JOM, in press (Sept. 2005).

[Bringa, 2005c] Bringa et al., Science, in press, (2005)

[Budil, 1997] K. S. Budil, T. S. Perry, S. A. Alvarez, D. Hargrove, J. R. Mazuch, A. Nikitin, and P. M. Bell, *Rev. Sci. Instrum.*, 1997, Vol. 68, 796.

[Cao, 2005] Bu Yang Cao, MSE (2005).

[Celliers, 1998] P. M. Celliers, G. W. Collins, L. B. Da Silva, D. M. Gold, and R. Cauble, *App. Phys. Lett.*, 1998, Vol. 73, 1320.

[Chen, 1996] S.R. Chen and G.T. Gray, *Metallurgical and Materials Transactions A-Physical Metallurgy and Materials Science*, 1996, Vol. 27, 2994.

[Colvin, 2003] J. Colvin, M. Legrand, B.A. Remington, G. Schurtz, and S.V. Weber, *J. Applied Phys.*, 2003, Vol. 93, 5287.

[Crozier, 1980] E.D. Crozier and A.J. Seary, Can. J. Phys., 1980, Vol. 58, 1388.

[Hayes, 2004] D. B. Hayes, C. A. Hall, J. R. Asay, and M. D. Knudson, J. Appl. Phys., 2004, Vol. 96, 5520.

[Dorn, 1964] J.E. Dorn and S. Rajnak, *Trans. Met. Soc. AIME*, 1964, Vol. 230, 1052.

[Edwards, 2004] J Edwards, K T Lorenz, B A Remington, S Pollaine, J Colvin, D Braun, B F Lasinski, D Reisman, J McNaney, J A Greenough, R Wallace, H Louis, and D Kalantar, Phys. Rev. Lett., 2004, Vol. 92, p. 075002.

[Follansbee, 1988] P.S. Follansbee and U.F. Kocks, *Acta Metall.*, 1988, Vol. 36, 81.

[Frost, 1982] Harold J. Frost and Michael F. Ashby, *Deformation-Mechanism Maps, The Plasticity and Creep of Metals and Ceramics,* Pergamon Press, 1982.

[Guyot, 1967] P. Guyot and J.E. Dorn, *Can. J. Phys.*, 1967, Vol. 45, 983.

[Hawreliak, 2005] J. Hawreliak, private commun. (2005).

[Hirth, 1982] John P. Hirth and Jens Lothe, *Theory of Dislocations*, 2nd Edition, Krieger Publishing Co., 1982.

[Hogan, 2001] W.J. Hogan, E.I. Moses, B.E. Warner, M.S. Sorem et al., *Nuclear Fusion*, 2001, Vol. 41, 567.

[Hoge, 1977] K.G. Hoge and A.K. Mukherjee, *J. Mat. Sci.*, 1977, Vol. 12, 1666.

[Hull, 1984] D. Hull and D.J. Bacon, *Introduction to Dislocations*, 3rd Edition, Butterworth-Heinemann, 1984.

[Ivanov, 2003] Dmitriy S. Ivanov, Leonid V. Zhigilei, Eduardo M. Bringa, Maurice De Konig, Bruce A. Remington, Maria Jose Caturla, and Stephen M. Pollaine, in press, *Proceedings of APS Topical Group on Shock Compression of Condensed Matter*, 2003.

[Ivanov, 2003] D. Ivanov and L. Zhigilei, *Phys. Rev. Lett.*, 2003, Vol. 91(10), 5701; *Phys. Rev. B*, 2003, Vol. 68 (6), 4114.

[Johnson, 1983] G.R. Johnson, J.M. Hoegfeldt, U.S. Lindholm, and A. Nagy, ASME *J. Eng. Mater. Tech.*, 1983b, Vol. 105, 42.

[Kalantar, 1999] D.H. Kalantar, B.A. Remington, E.A. Chandler, J.D. Colvin, D. Gold, K. Mikaelian, S.V. Weber, L.G. Wiley, J.S. Wark, A.A. Hauer, and M.A. Meyers, *Journal of Impact Engineering*, 1999, Vol. 23, 409.

[Kalantar, 2000] D.H. Kalantar, B.A. Remington, J.D. Colvin, K.O. Mikaelian, S.V. Weber, L.G. Wiley, J.S. Wark, A. Loveridge, A.M. Allen, A. Hauer, and M.A. Meyers, *Phys. Plasmas*, 2000, Vol. 7, 1999.

[Kalantar, 2001] D. H. Kalantar, A. M. Alien, F. Gregori, B. Kad, M. Kumar, K. T. Lorenz, A. Loveridge, M. A. Meyers, S. Pollaine, B. A. Remington, and J. S. Wark, *Proceedings of the APS SCCM* 2001, AIP Vol 620, pp. 615-618.

[Kalnatar, 2003] D.H. Kalantar, J. Belak, E. Bringa, K. Budil, M. Caturla, J. Colvin, M. Kumar, K. T. Lorenz, R. E. Rudd, and J. Stolken A. M. Allen, K. Rosolankova, and J. S. Wark, M. A. Meyers and M. Schneider, *Phys. Plasmas*, 2003, 10, 1569.

[Kalantar, 2005] D.H. Kalantar et al., Phys. Rev. Lett., in press (2005).

[Kochs, 1975] U.F. Kocks, A.S. Argon, and M.F. Ashby, *Thermodynamics and Kinetics of Slip,* Pergamon Press, 1975.

[Konningsberger, 1988] D.C. Konningsberger and R. Prins, *X-ray Absorption: Principles, Applications, Techniques of EXAFS, SEXAFS, and XANES,* John Wiley & Sons, 1988.

[Kumar, 1968] A. Kumar, F.E. Hauser, and J.E. Dorn, Acta Met., 1968, Vol. 16, 1189.

[Kadau, 2002] Kai Kadau, Timothy C. Germann, Peter S. Lomdahl, Brad Lee Holian, Science 296, 1681 (2002).

[Lee, 1981] P.A. Lee, P.H. Citrin, P. Eisenberger, and B.M. Kincaid, Rev. Mod. Phys., 1981, Vol. 53, 769.

[Lipkin, 1977] J. Lipkin and J.R. Asay, J. Appl. Phys., 1977, Vol. 48, 182.

[Lorenz, 2005] K.T. Lorenz, LLNL, L-021, Livermore, CA, 94550, private communication.

[Lorenz, 2005a] K.T. Lorenz et al., PoP 12, 056309 (2005)

[Lorenz, 2005b] Lorenz, J. Appl. Phys., submitted. (2005)

[Loveridge, 2001] A. Loveridge-Smith, A. Allen, J. Belak, T. Boehly, A. Hauer, B. Holian, D. Kalantar, G. Kyrala, R.W. Lee, P. Lomdahl, M. A. Meyers, D. Paisley, S. Pollaine, B. Remington, D. C. Swift, S. Weber, and J.S. Wark, Phys. Rev. Lett., 2001, Vol. 86 (11), 2349.

[McNaney, 2004] J. M. McNaney, J. Edwards, R. Becker, T. Lorenz, B. Remington, *Metall. Mater. Trans. A*, 2004, Vol. 35A, 2625.

[McNaney, 2005] J. M. McNaney, B. Torralva, J. S. Harper, K. T. Lorenz, B. A. Remington, M. S. Schneider, and M. Wall, Acta Materialia, submitted (2005).

[Meyers, 2002] M.A. Meyers, D.J. Benson, O. Vohringer, B.K. Kad, Q. Xue, and H.-H. Fu, *Mat. Sci. Eng.* 2002, Vol. A322, 194.

[Meyers, 1981] Marc A. Meyers and Lawrence E. Murr, *Shock Waves and High-Strain-Rate Phenomena in Metals: Concepts and Applications,* Plenum Press, 1981.

[Meyers, 1994] Marc A. Meyers, *Dynamic Behavior of Materials,* 1994, John Wiley & Sons, Inc.

[Meyers, 2003] M.A. Meyers, F. Gregori, B.K. Kad, M.S. Schneider, D.H. Kalantar, B.A. Remington, G. Ravichandran, T. Boehly, and J.S. Wark, *Acta Mat.* 2003, Vol. 51, 1211.

[Mikaelian, 1996] K. Mikaelian, *Phys. Rev. E*, 1996, Vol. 54, 3676.

[Murr, 1981] L.E. Murr, in *Shock Waves and High-Strain-Rate Phenomena in Metals: Concepts and Applications* , Edited by Marc A. Meyers and Lawrence E. Murr, p. 607-673, Plenum Press, 1981.

[Paisner, 1994] J. A. Paisner, E. M. Campbell, W. J. Hogan, *Fusion Technol.*, 1994, Vol. 26, 755.

[Pollaine, 2005] S.M. Pollaine, private communication (2005).

[Preston, 2003] D.L. Preston, D.L. Tonks, and D.C. Wallace, J. Appl. Phys., 2003, Vol. 23, 211.

[Regazzoni, 1987] G. Regazzoni, U.F. Kocks, and P.S. Follansbee, *Acta Metall.*, 1987, Vol. 35, 2865.

[Rehr, 2000] J. Rehr and R.C. Albers, Rev. Mod. Phys., 2000, Vol. 72, 621.

[Remington 2005a] B.A. Remington, G. Bazan, J. Belak, E. Bringa, M. Caturla, J.D. Colvin, M.J. Edwards, S.G. Glendinning, D. Ivanov, B. Kad, D.H. Kalantar, M. Kumar, B.F. Lasinski, K.T. Lorenz, J.M. McNaney, D.D. Meyerhofer, M.A. Meyers, S.M. Pollaine, D. Rowley, M. Schneider, J.S. Stölken, J.S. Wark, S.V. Weber, W.G. Wolfer, B. Yaakobi, and L. Zhigilei, Met. Mat. Trans. A, 2004, VOL. 35A, p. 2587.

[Remington, 2005b] B.A. Remington et al., Astrophys. Space Science 298, 235 (2005).

[Rosolankova, 2004] K. Rosolankova *et al.*, "X-ray diffraction from shocked crystals: experiments and predictions of molecular dynamics simulations," in *Shock Compression of Condensed Matter-2003*, Ed. M.D. Furnish,Y.M. Gupta, and J.W. Forbes (AIP, 2004), p. 1195.

[Sadigh, 2005] Babak Sadigh et al., in prep. (2005).

[Schneider, 2004] M. S. Schneider, B. K. Kad, F. Gregori, D. Kalantar, B. A. Remington, and M. A. Meyers, *Metall. Mater. Trans. A*, 2004, Vol. 35A, 2633.

[Schneider, 2005a] M.S. Schneider, Mat. Sci. Forum (2005).

[Schneider, 2005b] M.S. Schneider, Int'l J.Imp.Eng. (2005).

[Steinberg, 1989] D.J. Steinberg and C.M. Lund, *J. Appl. Phys*, 1989, Vol. 65, 1528.

[Steinberg, 1980] D.J. Steinberg, S.G. Cochran, and M.W. Guinan, *J. Appl. Phys*, 1980, Vol. 51, 1496.

[Swegle, 1983] J.W. Swegle and D.E. Grady, *J. Appl. Phys*., 1983, Vol. 58, 941.

[Swift, 2005] Swift et al., PoP 12, 056308 (2005).

[Tas, 1994] G. Tas and H. J. Maris, *Phys. Rev. B*, 1994, Vol. 49**,** 15046.

[Wolfer, 1999] W.G. Wolfer, LLNL Internal Report No. UCRL-ID-136221, Nov. 1999.

[Yaakobi, 2003] B. Yaakobi, F. J. Marshall, T. R. Boehly, R. P. J. Town, and D. D. Meyerhofer, *J. Optical Soc. America B-Optical Physics*, 2003, Vol. 20, 238.

[Yaakobi, 2004a] B. Yaakobi, D. D. Meyerhofer, T. R. Boehly, J. J. Rehr, R. C. Albers, B. A. Remington, and S. Pollaine, Phys. Rev. Lett., 2004, Vol. 92, p. 095504.

[Yaakobi, 2004b] B. Yaakobi, D. D. Meyerhofer, T. R. Boehly, J. J. Rehr, B. A. Remington, P.G. Allen, S. Pollaine, and R. C. Albers, Phys. Plasmas, 2004, Vol. 11, p. 2688.

[Yaakobi, 2005a] B. Yaakobi et al., Phys. Rev. Lett. 95, 075501 (2005).

[Yaakobi, 2005b] Yaakobi, PoP, in press (2005).

[Zerilli, 1987] F.J. Zerilli and R.W. Armstrong, *J. Appl. Phys*., 1987, Vol. 61, 1816;

[Zerilli, 1990] F.J. Zerilli and R.W. Armstrong, J. Appl. Phys., 1990, Vol. 68, 915.

[Zhou, 2001] X.W. Zhou, H.N.G. Wadley, R.A. Johnson, D.J. Larson, N. Tabat, A. Cerezo, A.K. Petford-Long, G.D.W. Smith, P.H. Cllifton, R.L. Martens, and T.F. Kelly, *Acta Mater*., 2001, Vol. 49, 4005.

[Zimmerman, 1975] G B. Zimmerman and W. L. Kruer, Comments Plasma Phys. Controlled Fusion 2, 51 (1975).

FIGURE CAPTIONS

Figure 1: Constitutive models. (a) Sketch showing schematically the mechanisms of stress assisted thermal activation and phonon drag deformation. (b) Flow stress (kbar) versus log strain rate for a variety of models (see text for details) for Ta at 0.5 Mbar, 500 K temperature, and plastic strain of 0.1: (1a) Hoge-Mukherjee, (1b) Steinberg-Lund, (2a) "hybrid" Steinberg-Lund, (2b) modified Steinberg-Lund, turning off phonon drag, and scaling the Peierls barrier with the pressure dependent shear modulus, and (3) the PTW model. (c) Flow stress vs. log strain rate for the PTW model for Ta at nominal 0.5 Mbar conditions, varying the temperature by 20% and 40%. (d) Same as (c) except the density was varied by 20% and 40%. [Remington, 2004]

Figure 2: Ramped drive. (a) Sketch of how the laser driven ramped drive works. (b) VISAR trace of a P_{max} = 1.2 Mbar ramped drive laser shot on the Omega laser. (c) Analysis of a series of 1.2 Mbar ramped drive experiments at Omega, varying the thickness of the Al sample. (d) Pressure vs. time for five different experiments at Omega, showing the ramped drive for maximum pressures spanning 0.15 kbar to 2 Mbar. [Edwards, 2004; Lorenz, 2005b]

Figure 3: RT as a strength diagnostic. (a) Experimental configuration for using the ramped drive at the Omega laser to do a Rayeligh-Taylor (RT) instability experiment at high pressure, solid state conditions. The unloading reservoir pushes on a rippled thin metal payload. (b) Examples of a series of RT experiments in Al6061-T6 to infer strength at P_{max} = 200 kbar. The 2D simulations used the Steinberg-Guinan strength model, and varied the pressure hardening term multiplier, A, until the results reproduced the experimental observations. [Lorenz, 2005a]

Figure 4: Parameters from the 2D RT simulations, volume averaged over the foil dimensions, assuming e^{-kz} weighting, where $k = 2\pi/\lambda$ is the perturbation wave vector (see text). Strength increased 4x due to pressure hardening. [Pollaine, 2005]

Figure 5: Extended x-ray absorption fine structure (EXAFS) measurement technique. (a) Physics basis for the EXAFS process. [Yaakobi, 2003] (b) Experimental configuration for the dynamic EXAFS technique, developed at the Omega laser. (c) X-ray spectrum emerging from the capsule implosion, used for the EXAFS transmission measurements. (d) Modulations above the K-edge of cold-Ti in an EXAFS demonstration experiment. [Yaakobi, 2003]

Figure 6: EXAFS results for (a) shocked V, and (b) shocked Ti, at $P_{shk} \sim 400$ kbar. (c) FEFF8 simulations of EXAFS from unshocked and shocked Fe, and (d) dynamic EXAFS measurements of unshocked and shocked Fe at $P_{shk} = 350$ kbar. [Yaakobi, 2004a, 2004b, 2005a, 2005b]

Figure 7: Dynamic diffraction technique. (a) Experimental configuration for laser based dynamic diffraction. (b) Example of dynamic diffraction on unshocked, single crystal Cu. (c) Example of dynamic diffraction from shocked (Pshk ~ 70 kbar) single crystal Ti. [Loveridge-Smith, 2001; Hawreliak, 2005; Swift, 2005; Lorenzana, 2005]

Figure 8: Molecular dynamics (MD) simulations. (a) A very large scale MD result of shocked single crystal Cu. [Bringa, 2005] (b) Analysis of the MD result shown in (a) to extract dislocation densitiy versus position at a variety of time steps (62, 72, 82, 10, and 143 psec). (c) The result of an MD simulations of shocked single crystal Ti. The colors represent coordination number. [Sadigh, 2005] (d) The pressure versus position for the

shocked Ti MD simulation shown in (c). Note the 3-wave structure: elastic, plastic, and phase transition waves.

Figure 9: Recovery and crater formation. (a) Experimental configuration for the laser based, ramped loading recovery experiments. (b) Typical crater result in ramp loaded single crystal Cu. (c) Results from 2D simulations showing pressure versus time and crater depth vs. time, for the experiment shown in (b). (d) Temperature vs. depth into the Cu sample, for the loading profile shown in (c). [McNaney, 2004; 2005]

Figure 10: (a)-(d) Recovery and TEM analysis. (a) Single crystal Cu, shocked along [100] at P_{shk} ~ 120 kbar = 12 GPa. (b) Similar to (a) expect that P_{shk} ~ 400 kbar = 40 GPa. (c) Similar to (b) expect that the 40 GPa shock was in the crystal [134] direction, instead of [100]. (d) Similar to (a) expect that the sample was single crystal Cu-6wt % Al, to lower the stacking fault energy. [Meyers, 2003; Schneider, 2004, 2005a, 2005b]. (e) Analytic model of the slip twinning threshold; and (f) residual dislocation density as a function of shock strength, and stacking fault energy. [Schneider, 2005b]

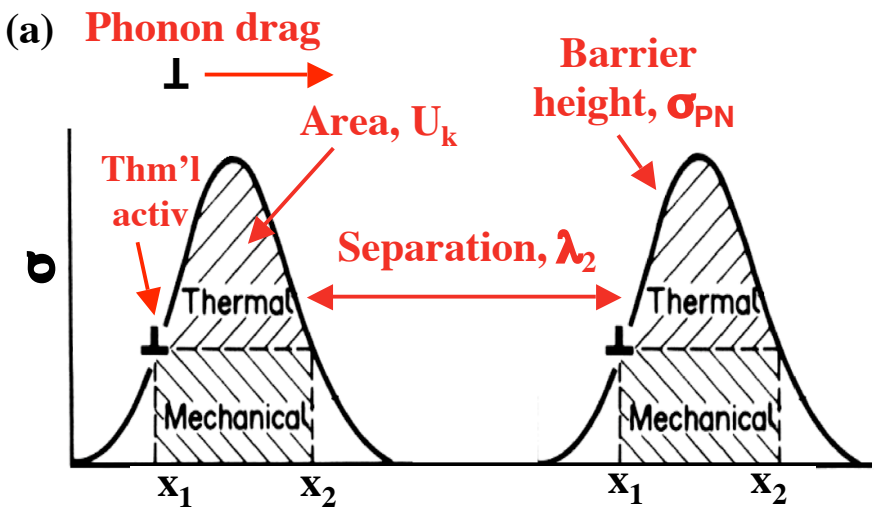

[M.A. Meyers text (1994)]

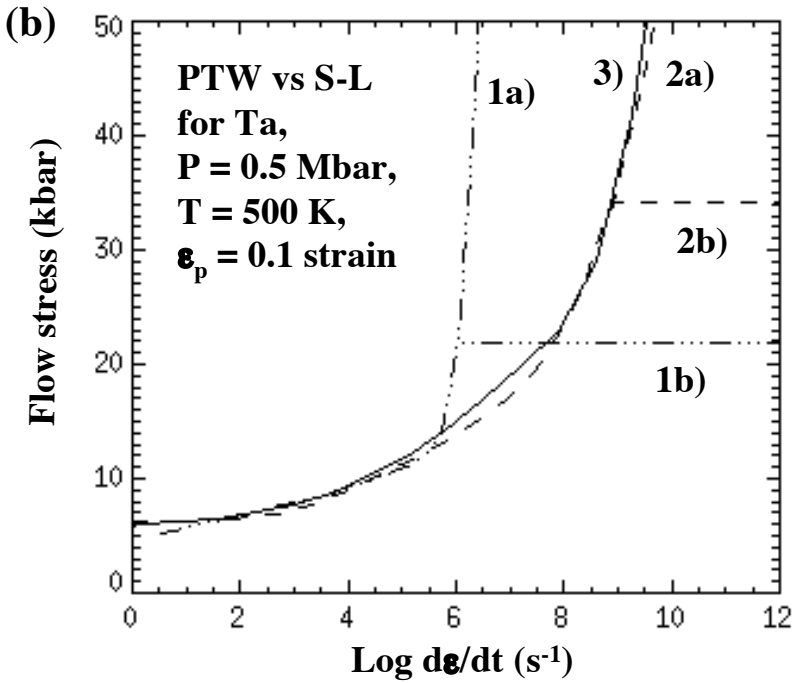

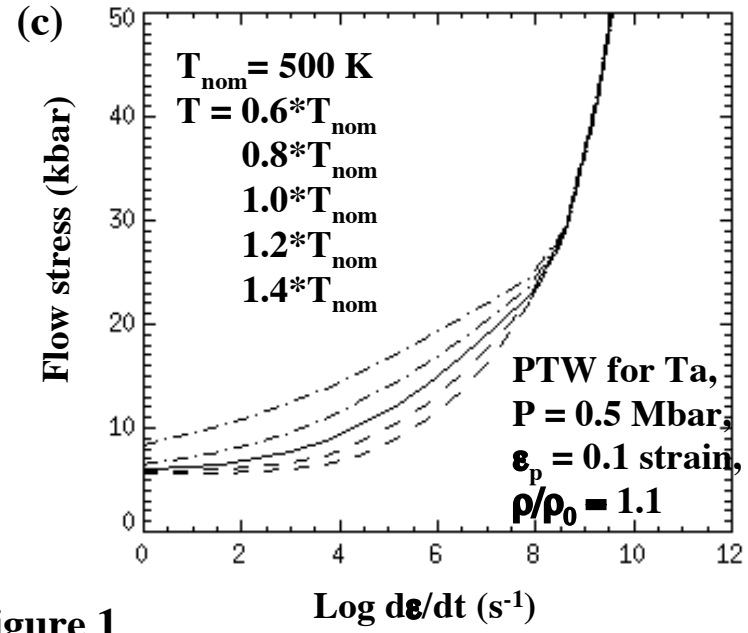

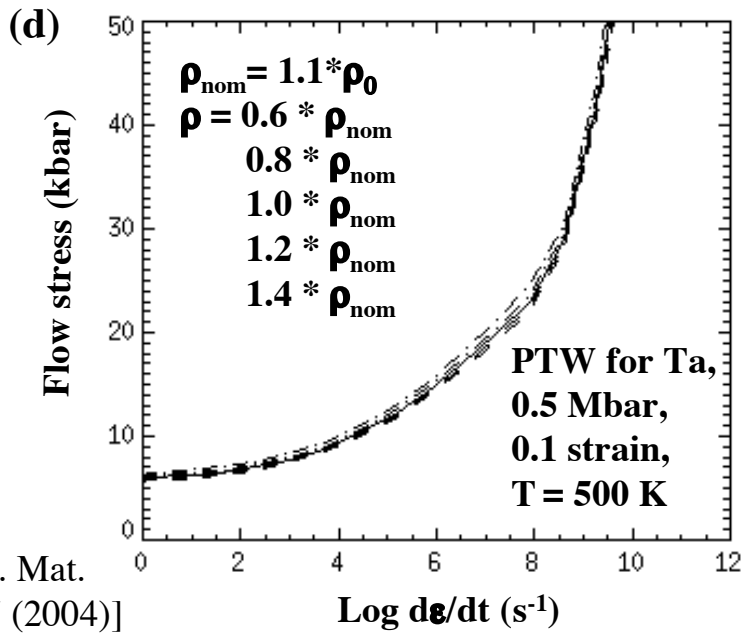

[Remington, Met. Mat. Trans. 35A, 2587 (2004)]

Figure 1

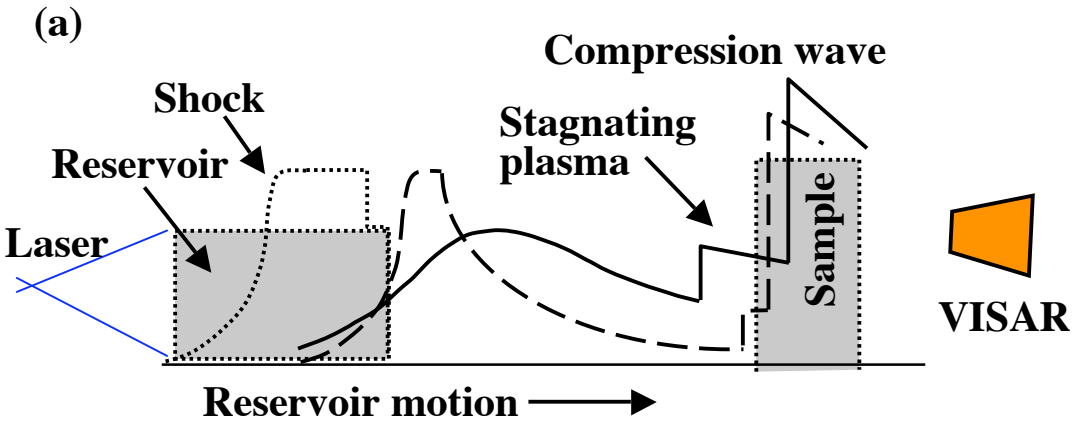

[Edwards et al., PRL 92, 075002(2004)]

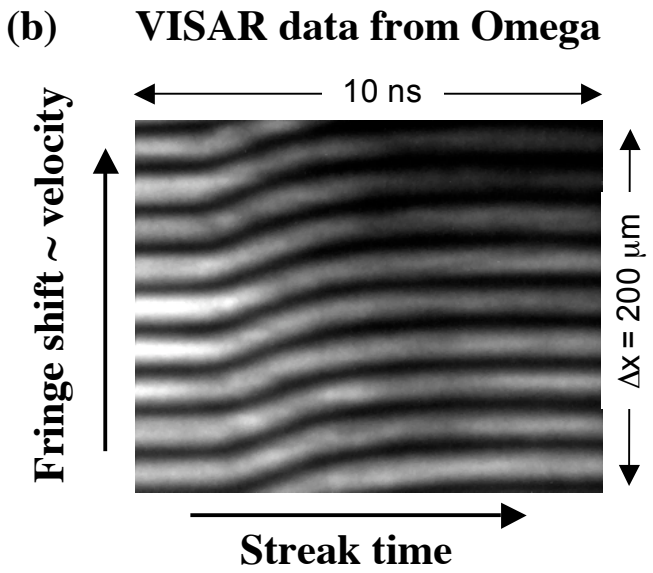

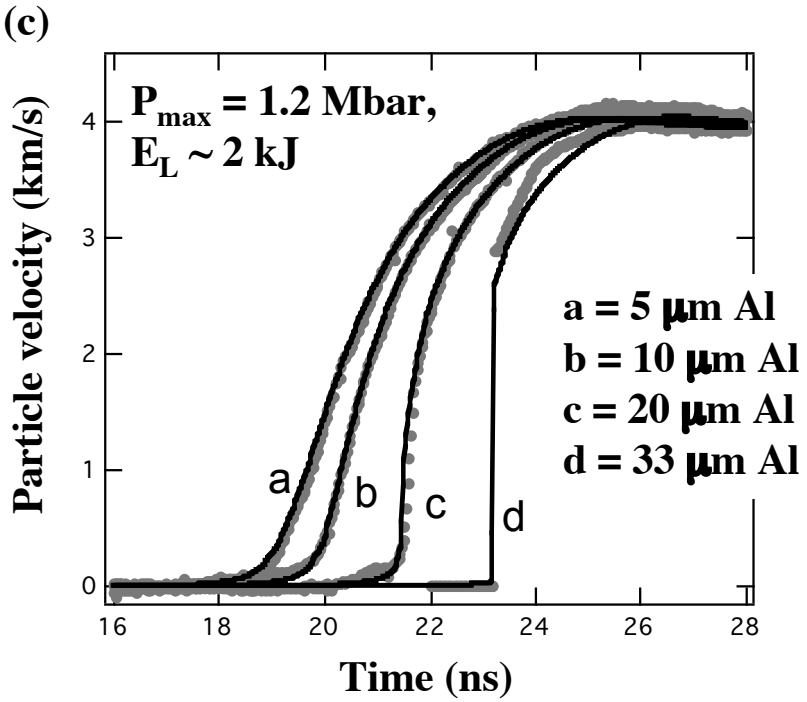

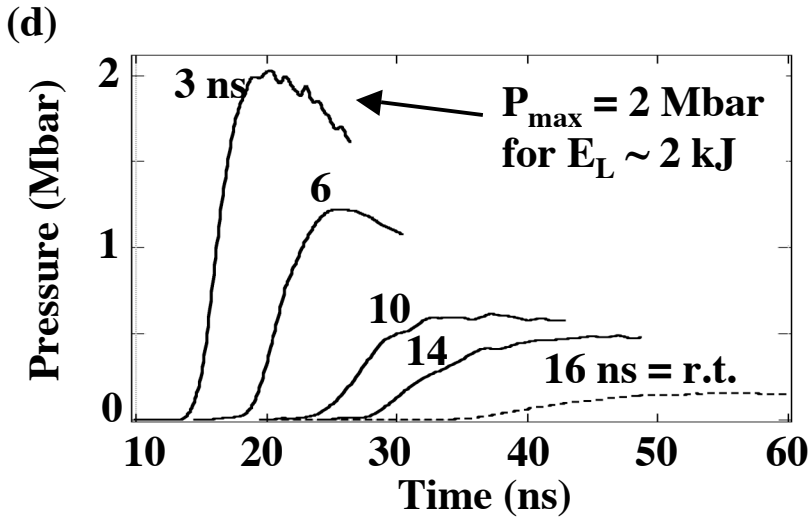

Figure 2

[Lorenz, J. Appl. Phys., submitted. (2005)]

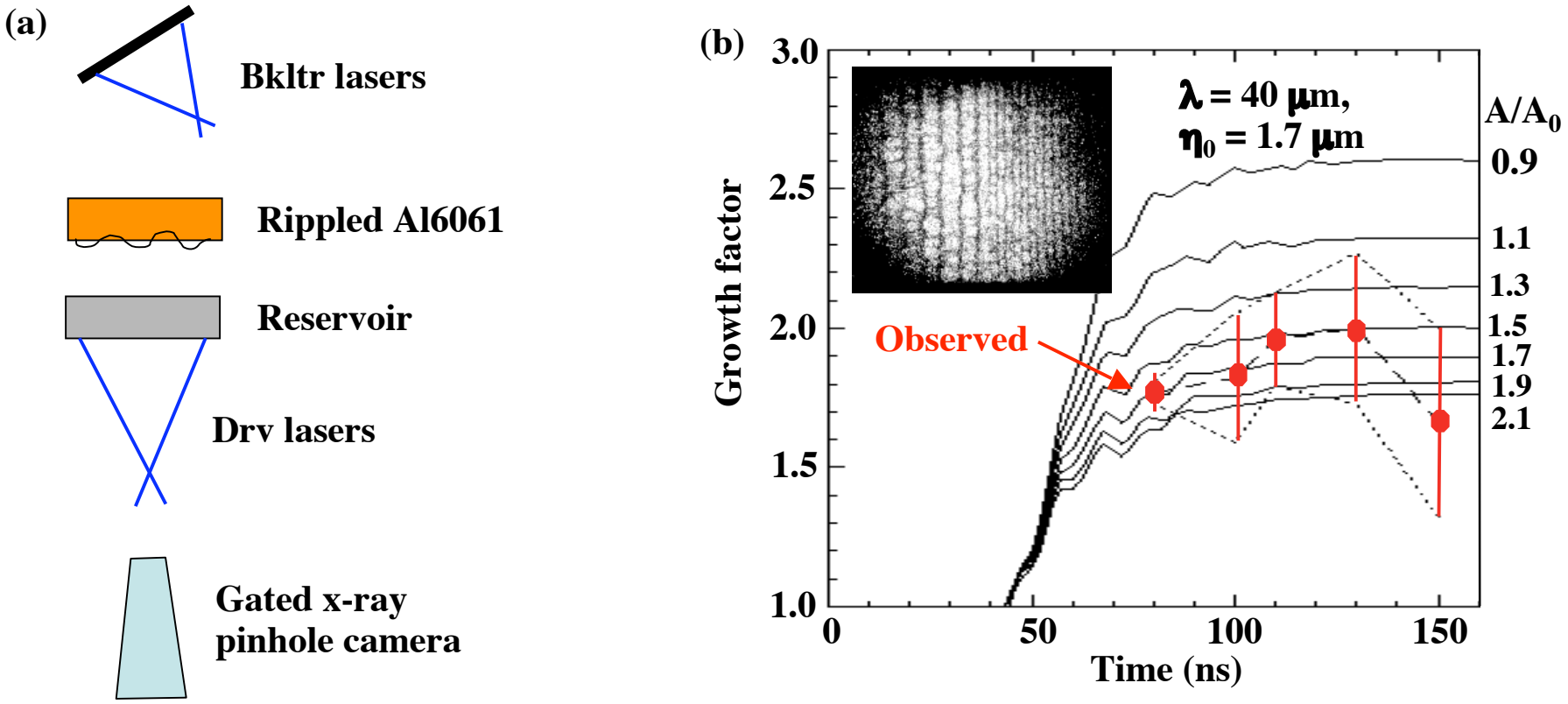

[K.T. Lorenz, Phys. Plasmas 12, 056309 (2005)]

Figure 3

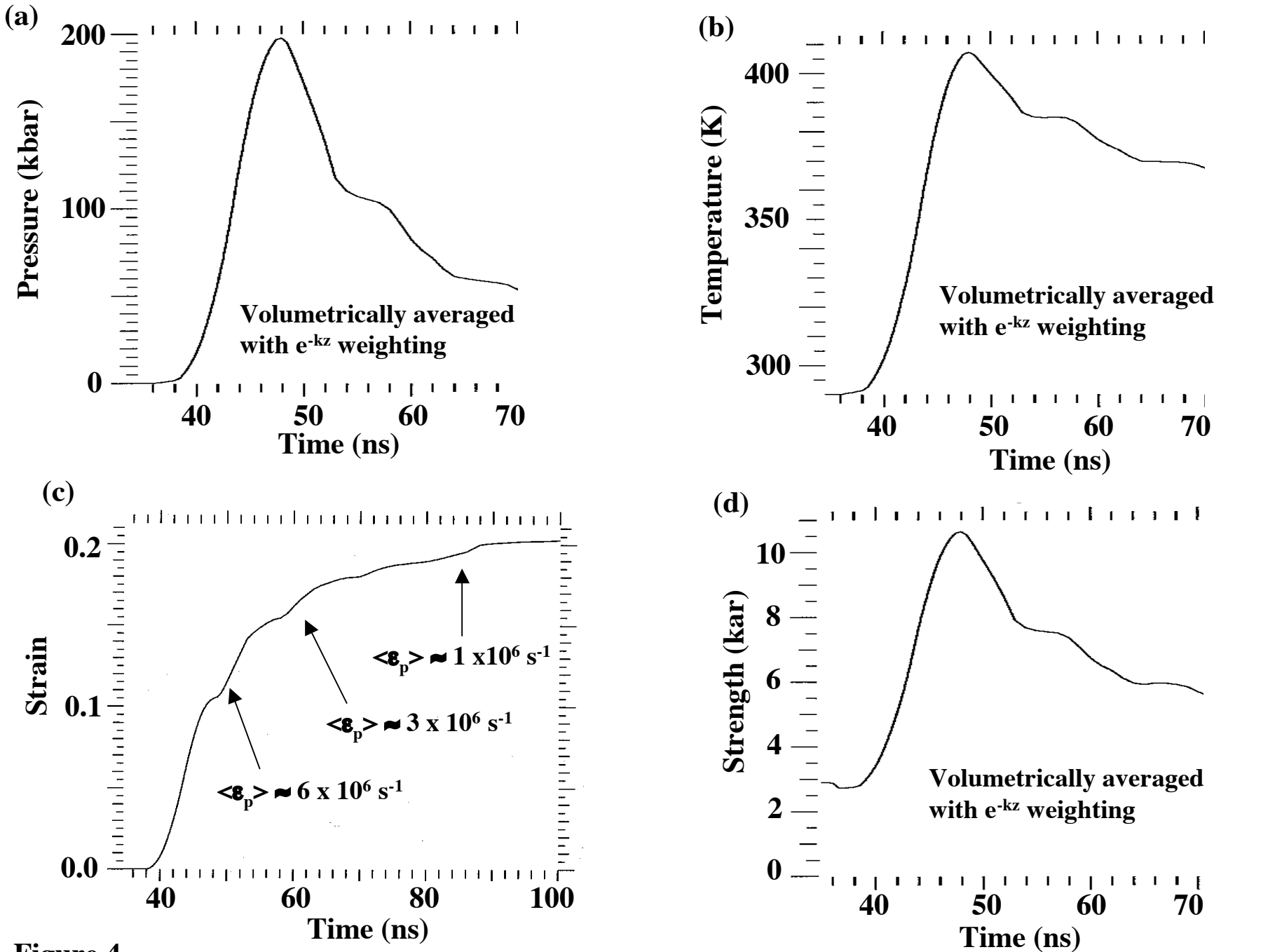

Figure 4

[Steve Pollaine 2D simulations]

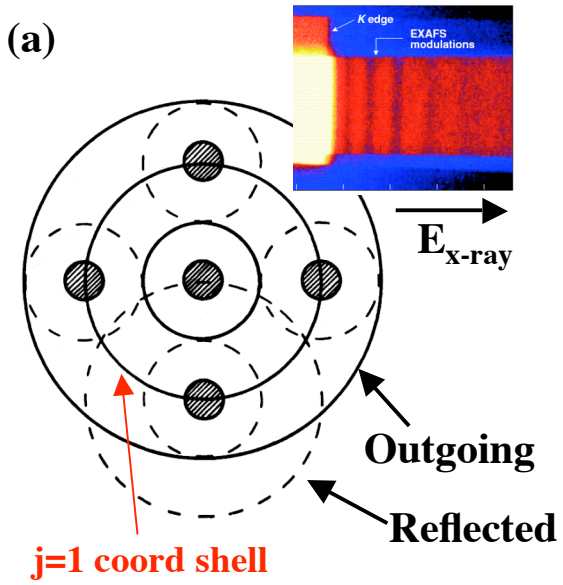

[D.C. Konningsberger, EXAFS text (1988)]

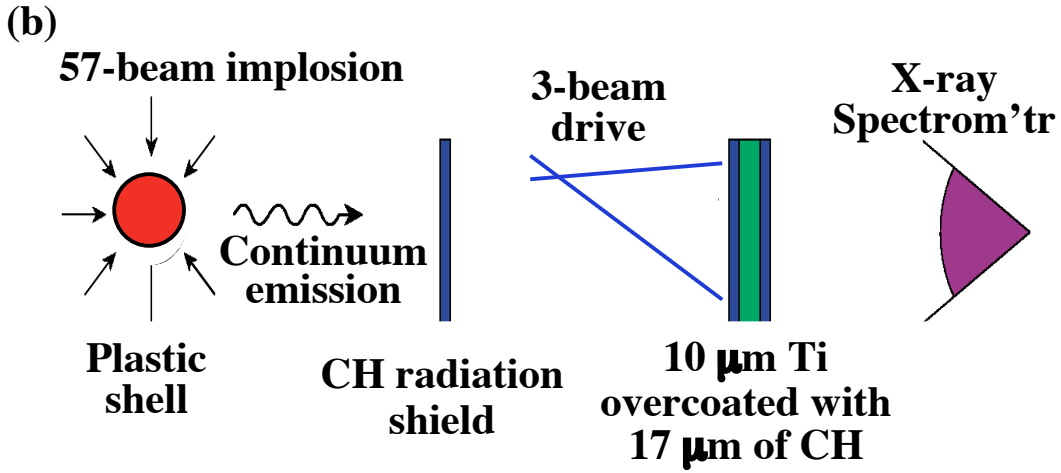

[Yaakobi, PRL 92, 095504 (2004);
Phys. Plasmas 11, 2688 (2004)]

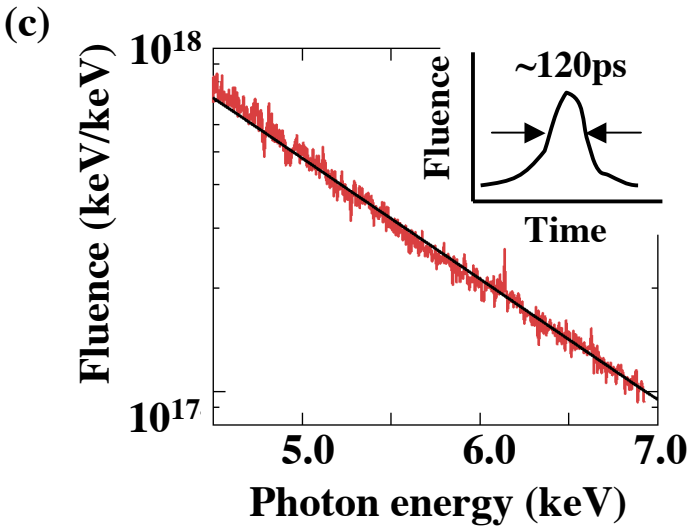

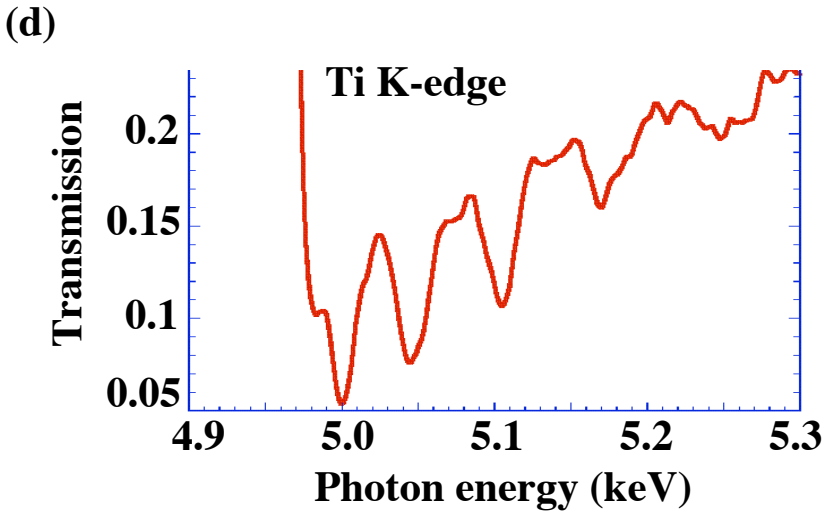

Figure 5

[Yaakobi, J. Opt. Soc. Am. B-Optical Phys. 20, 238 (2003)]

(a)

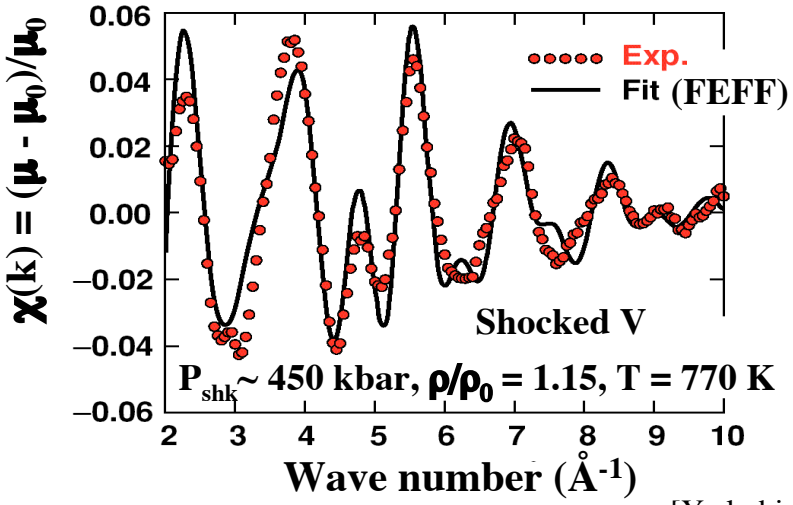

[Yaakobi, PRL 92, 095504 (2004); PoP 11, 2688 (2004)]

(b)

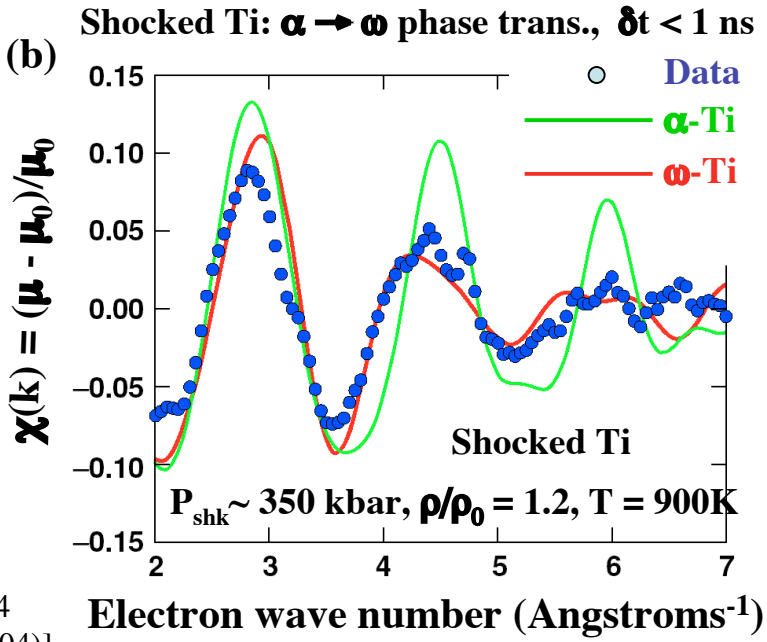

(c)

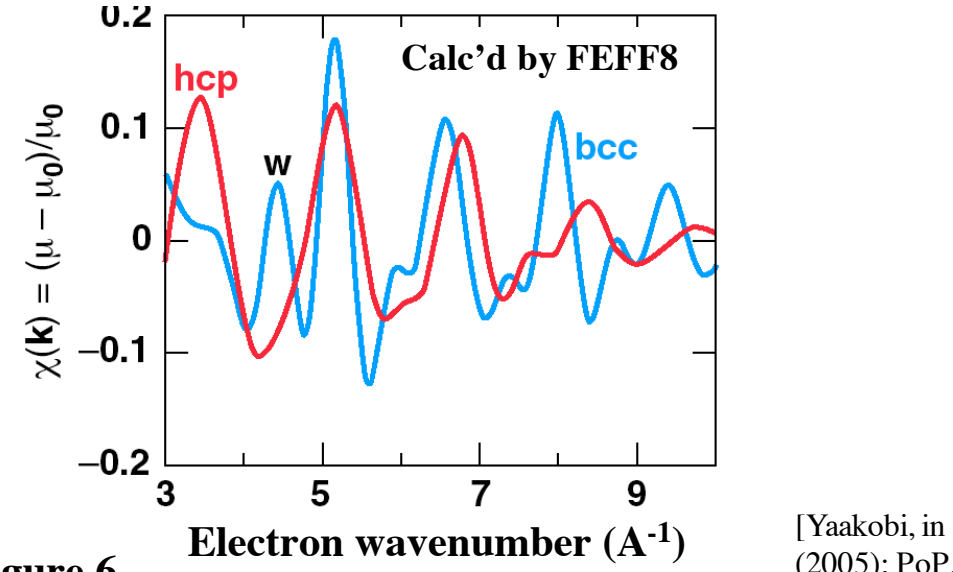

[Yaakobi, in press, PRL (2005); PoP, in press (2005)]

(d)

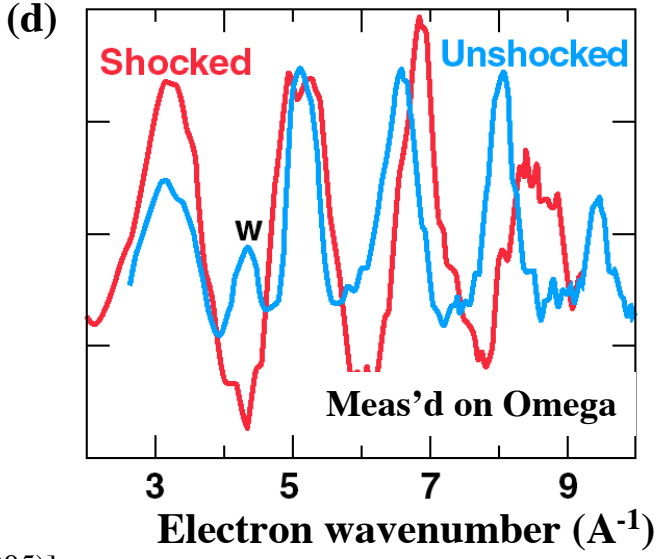

Figure 6

(a)

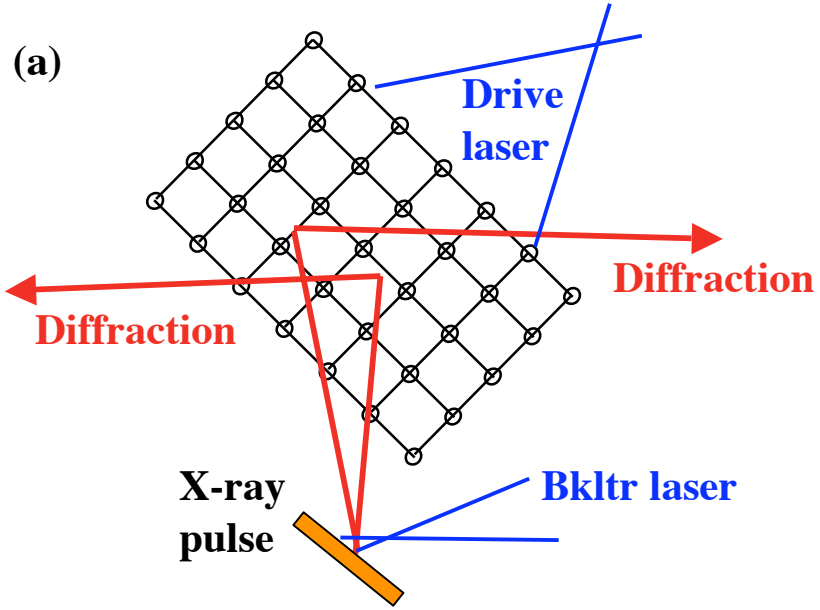

(b) **Single crystal, unshocked Cu, Vulcan laser**

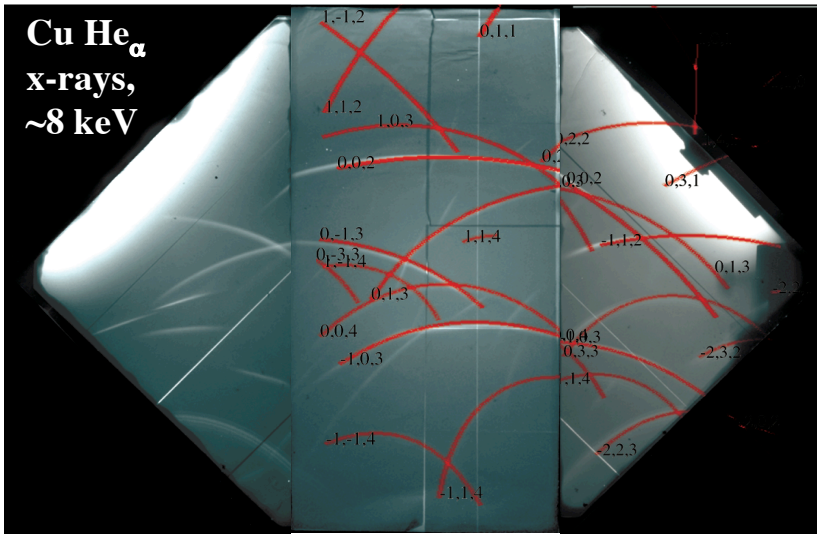

[Hawreliak, private commun. (2005);
Loveridge-Smith, PRL 86, 2349 (2001)]

(c) **Ti single crystal, shocked along [0002],
Janus laser, P_{shk}= 6.9 GPa**

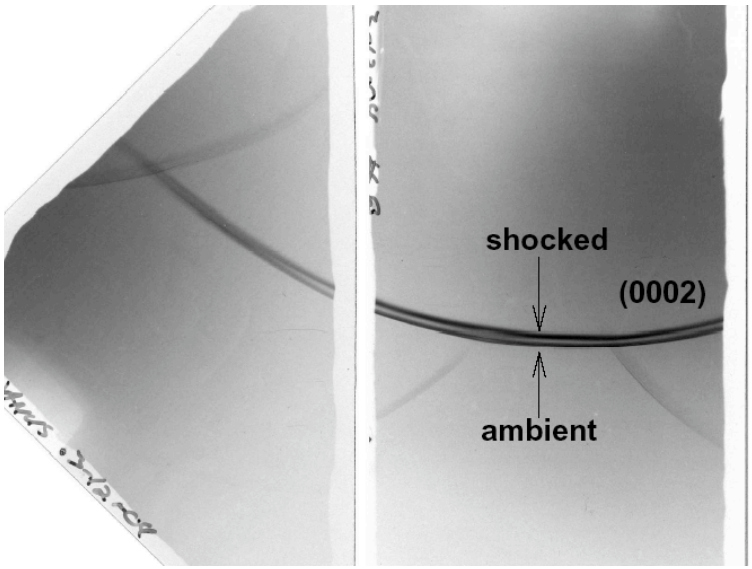

[Swift, PoP 12,
056308 (2005)]

Figure 7

MD simulation, ramped shock, single crystal Cu with sources

(a)

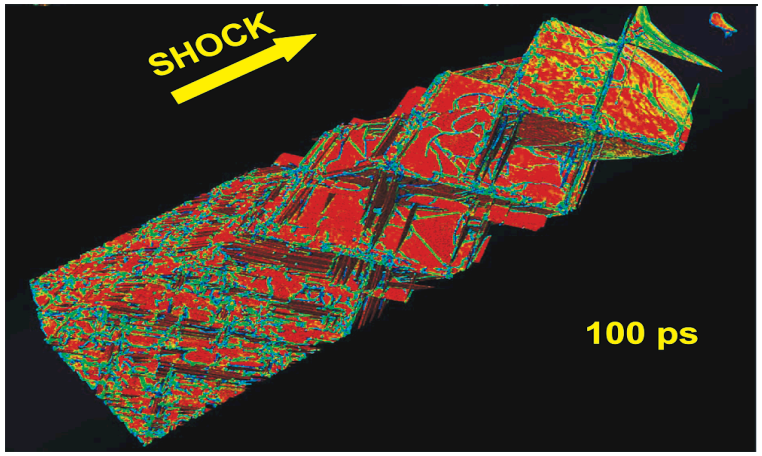

[Bringa, submitted, Nature (2005)]

(b)

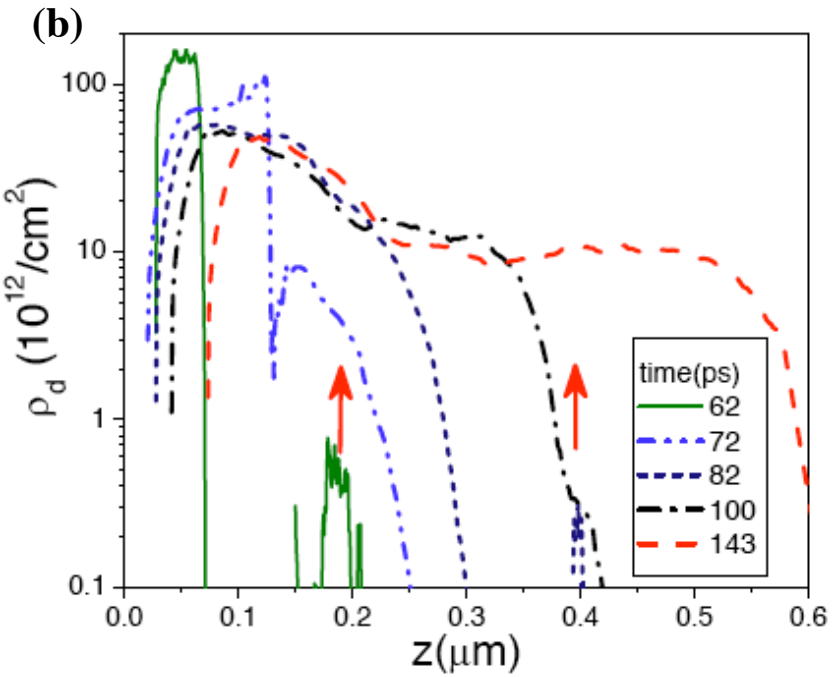

(c)

MD, ~220 kbar shock, single crystal Ti

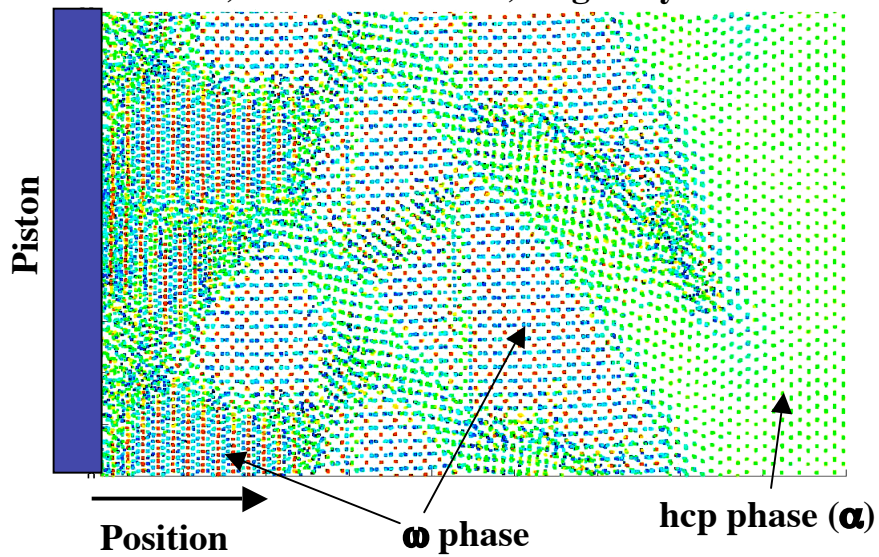

(d)

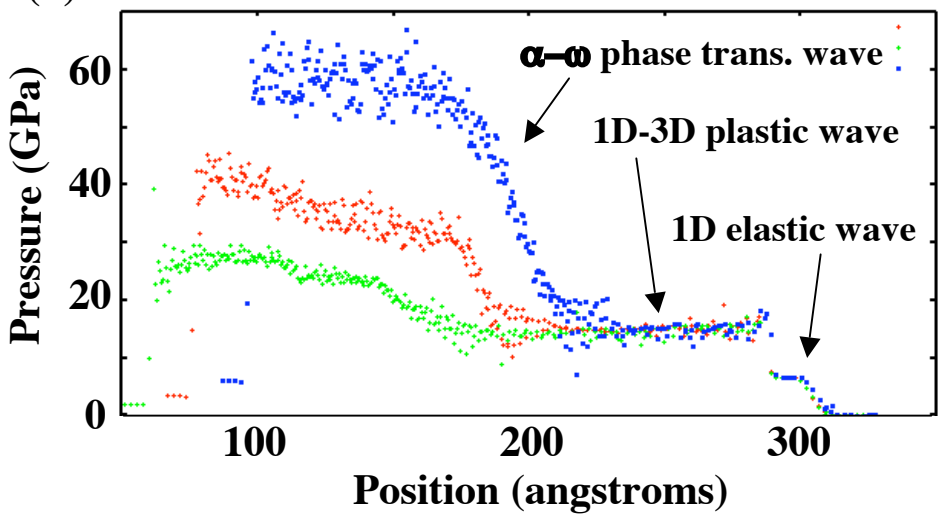

Figure 8

[Babak Sadigh et al., in prep. (2005)]

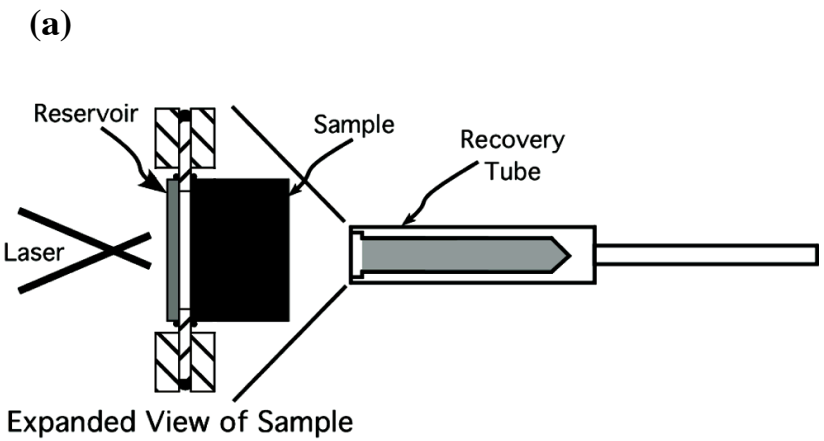

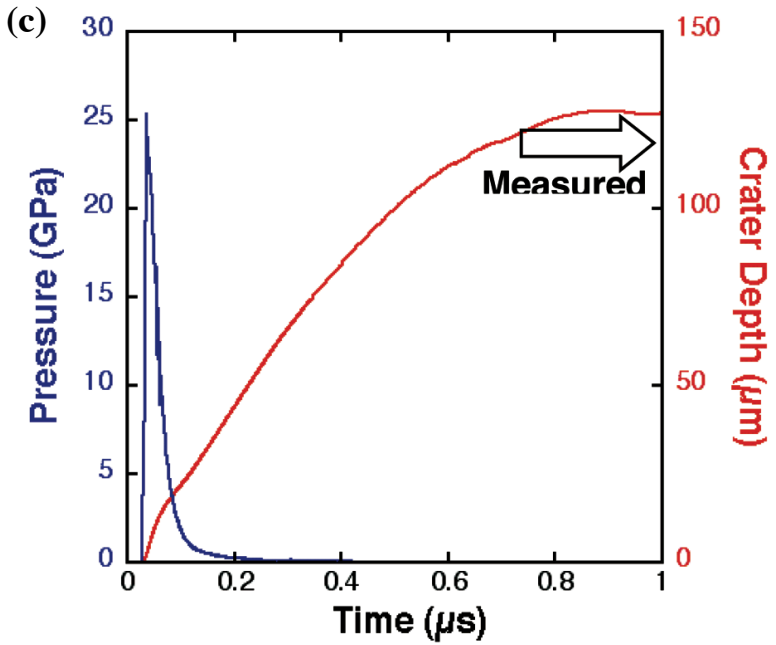

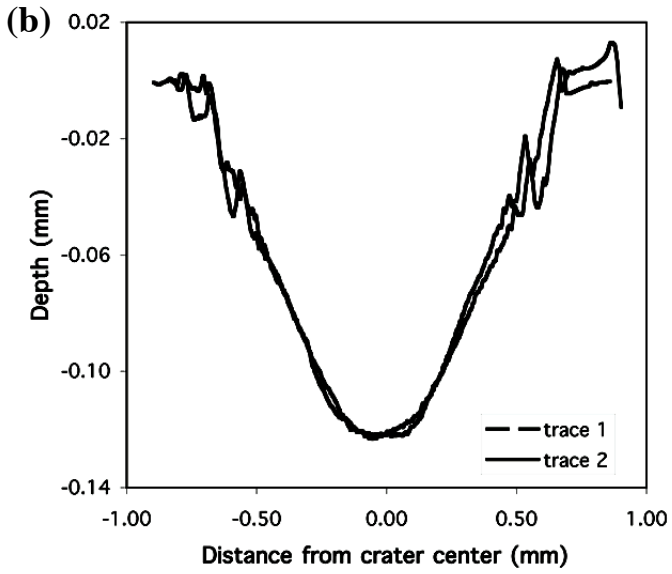

[McNaney, Acta Mat., submitted (2005)]

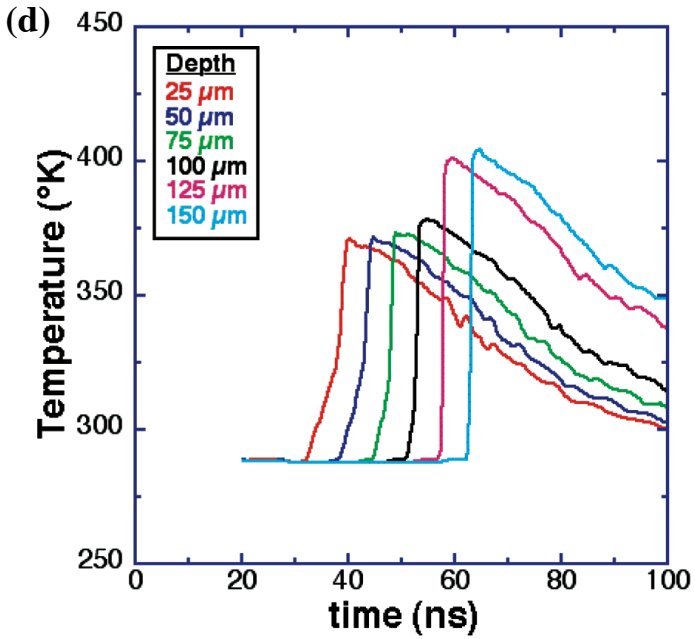

[McNaney, Acta Mat., submitted (2005)]

Figure 9

(a) **Slip at P_{shk}~ 12 GPa, Cu [100]**

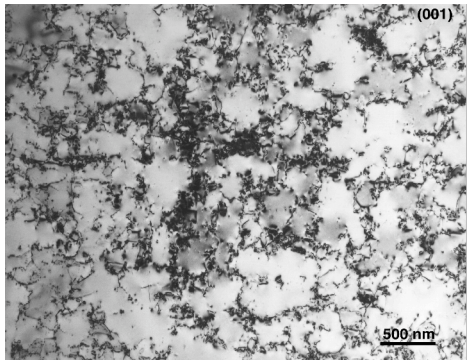

[M.A. Meyers, Acta Mat. 51, 1211 (2003]

(c) **Slip at P_{shk}~ 40 GPa, Cu [134]**

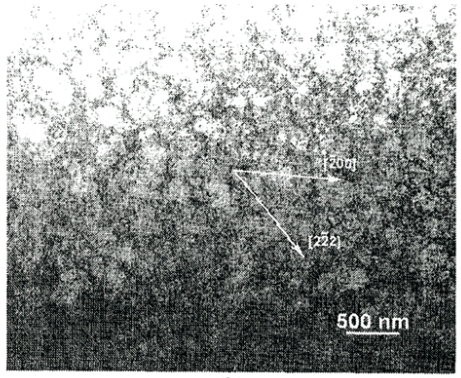

[M.S. Schneider, Met. Mat. Trans. A 35, 2633 (2004); Mat. Sci. Forum (2005)]

(e)

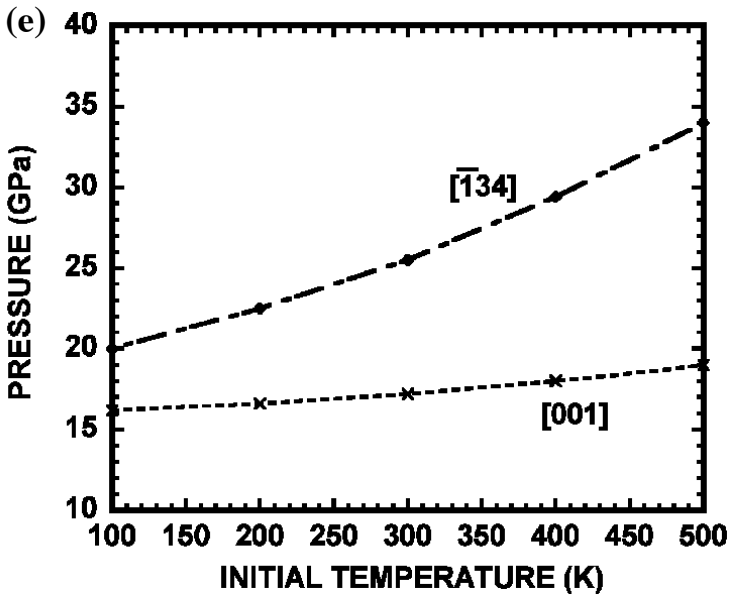

[Schneider, Met. Mat. Trans. A 35, 2633 (2004)]

(b) **Slip at P_{shk}~ 40 GPa, Cu [100]**

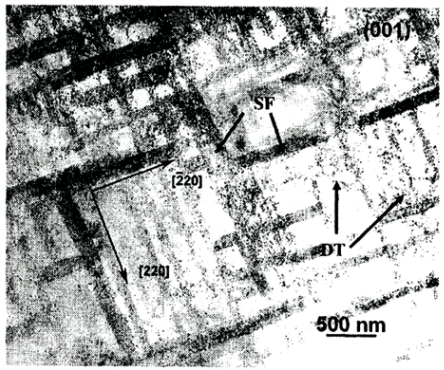

[M.A. Meyers, Acta Mat. 51, 1211 (2003]

(d) **P ~ 12 GPa, [100], Cu-6wt% Al**

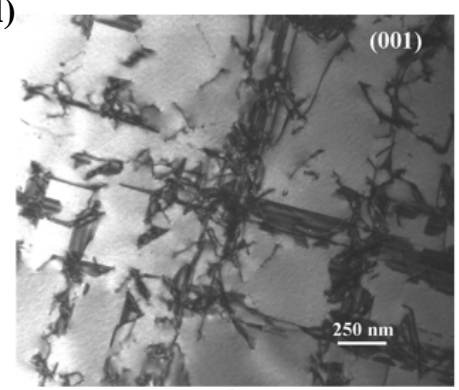

[M.S. Schneider, Int'l J.Imp.Eng. (2005)]

(f)

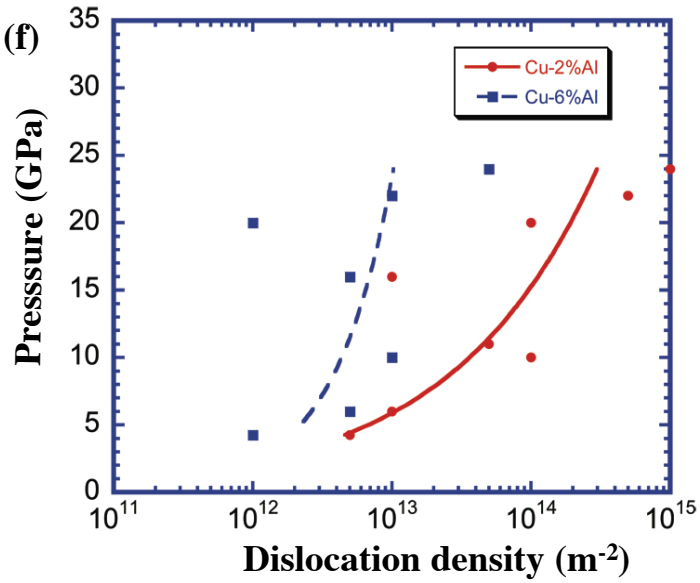

[M.S. Schneider, Int'l J.Imp.Eng. (2005)]

Figure 10